ACS APPLIED MATERIALS & INTERFACES

www.acsami.org Research Article

Design of Magnetic Fe_3O_4/CeO_2 "Core/Shell"-Like Nanocomposites with Pronounced Antiamyloidogenic and Antioxidant Bioactivity

Yuliia Shlapa,* Katarina Siposova, Katerina Veltruska, Valentin-Adrian Maraloiu, Ivana Garcarova, Michal Rajnak, Andrey Musatov,* and Anatolii Belous

Cite This: *ACS Appl. Mater. Interfaces* 2023, 15, 49346−49361 Read Online

ACCESS | Metrics & More | Article Recommendations

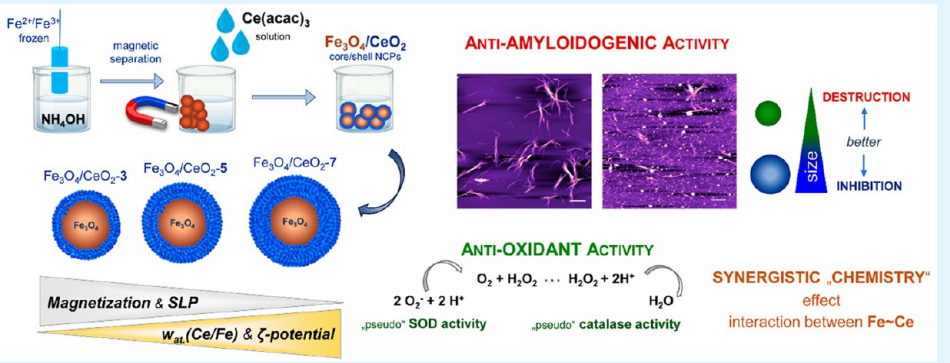

ABSTRACT: "Core/shell" nanocomposites based on magnetic magnetite (Fe_3O_4) and redox-active cerium dioxide (CeO_2) nanoparticles (NPs) are promising in the field of biomedical interests because they can combine the ability of magnetic NPs to heat up in an alternating magnetic field (AMF) with the pronounced antioxidant activity of CeO_2 NPs. Thus, this report is devoted to Fe_3O_4/CeO_2 nanocomposites (NCPs) synthesized by precipitation of the computed amount of "CeO_2-shell" on the surface of prefabricated Fe_3O_4 NPs. The X-ray diffraction, X-ray photoelectron spectroscopy, and high-resolution transmission electron microscopy data validated the formation of Fe_3O_4/CeO_2 "core/shell"-like NCPs, in which ultrafine CeO_2 NPs with an average size of approximately 3−3.5 nm neatly surround Fe_3O_4 NPs. The presence of a CeO_2 "shell" significantly increased the stability of Fe_3O_4/CeO_2 NCPs in aqueous suspensions: Fe_3O_4/CeO_2 NCPs with "shell thicknesses" of 5 and 7 nm formed highly stable magnetic fluids with ζ-potential values of >+30 mV. The magnetization values of Fe_3O_4/CeO_2 NCPs decreased with a growing CeO_2 "shell" around the magnetic NPs; however, the resulting composites retained the ability to heat efficiently in an AMF. The presence of a CeO_2 "shell" generates a possibility to precisely regulate tuning of the maximum heating temperature of magnetic NCPs in the 42−50 °C range and stabilize it after a certain time of exposure to an AMF by changing the thickness of the "CeO_2-shell". A great improvement was observed in both antioxidant and antiamyloidogenic activities. It was found that inhibition of insulin amyloid formation, expressed in IC_{50} concentration, using NCPs with a "shell thickness" of 7 nm was approximately 10 times lower compared to that of pure CeO_2. For these NCPs, more than 2 times higher superoxide dismutase-like activity was observed. The coupling of both Fe_3O_4 and CeO_2 results in higher bioactivity than either of them individually, probably due to a synergistic catalytic mechanism.

KEYWORDS: *magnetite, cerium dioxide, "core/shell" nanocomposites, synthesis, morphology, magnetization, specific loss power, antioxidant and antiamyloid activities*

1. INTRODUCTION

Detailed and in-depth research in the field of nanotechnology has become a large and important part of modern science. The transition to the "nanoscale" has changed the view of conventional materials because the properties of nanomaterials are entirely different from those in a bulk state,[1,2] which makes them attractive for use in the different fields of engineering and technology, as well as in medicine.[3,4]

Magnetic nanoparticles (NPs) are being studied especially intensively in the field of biomedicine (in cancer therapy, drug

Received: July 24, 2023
Accepted: September 28, 2023
Published: October 12, 2023

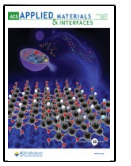

https://doi.org/10.1021/acsami.3c10845
ACS Appl. Mater. Interfaces 2023, 15, 49346−49361

delivery, etc.). The well-known magnetite (Fe_3O_4) with spinel structure can be an excellent carrier for the targeted delivery of various drugs and drug-like substances due to its strong magnetic properties.[5] In addition, as a response to applying an external alternating magnetic field (AMF), the Fe_3O_4 NPs can be effectively heated and, therefore, have great prospects in cancer treatment by magnetic hyperthermia and/or triggering the release of drugs from a thermally sensitive carrier.[6,7] Moreover, magnetic NPs could act as sonosensitizers, which can locally increase the attenuation of ultrasound waves within the tumor area. Thus, magnetic NPs can be applied as a material base for the use of synergetic effects of combined treatments (ultrasound and magnetic hyperthermia).[8,9] Within cancer treatment, the generation of reactive oxygen species (ROS) that trigger oxidative stress-induced tumor cell death can be enhanced by the presence of AMP-sensitive Fe_3O_4 NPs that can stimulate enzymes, producing ROS.[10] In addition, the application of an AMF leads to increased ROS production, which is proposed as one of the possible mechanisms of the magnetic hyperthermia treatment. As a consequence, the coapplication of Fe_3O_4 with an AMF can lead to the overproduction of ROS and the development of oxidative stress with further serious outcomes. Oxidative stress is thought to play a significant role in aging and age-related neurodegenerative disorders characterized by the presence of amyloid structures. Compelling evidence supports a tight link between oxidative stress and protein aggregation processes that are involved in the development of such neurodegenerative pathophysiological states. However, the exact mechanism and interplay between oxidative stress and amyloidosis are not known. Fe_3O_4-based NPs exhibit antiamyloid activity, and the ability to inhibit protein amyloid aggregate formation as well as the disassembly of preformed amyloid structures is observed to be size-, stability-, and surface-modification-dependent.[11−14]

In turn, due to their redox properties (mixed valence states), Fe_3O_4 NPs exhibit catalytic activity originating from Fenton-like reactions. However, surface oxidation of magnetite during Fenton reactions may lead to a gradual decrease in the catalytic reactivity. Moreover, magnetite particles tend to aggregate in aquatic environments, which may reduce the number of available surface-active sites for catalysis. Thus, it is important to enhance or stabilize the Fe_3O_4 NPs as well as their antioxidant properties. Cerium dioxide (CeO_2) NPs seem to be a suitable/promising choice because they are stable, biocompatible, and known as powerful antioxidants.[15−19] It was previously demonstrated that the antioxidant activity of CeO_2 NPs is closely linked to their physical−chemical properties, i.e., particle size and the percentage of Ce^{3+} ions on the NP surface.[20−22] Therefore, the fabrication of a composite based on Fe_3O_4 and CeO_2 NPs may lead to a product that will combine magnetic, antioxidant, and antiamyloid properties. Furthermore, the presence of CeO_2 on the surface of Fe_3O_4 NPs may protect magnetic NPs against their oxidation. On the other hand, the fabrication of Fe_3O_4/CeO_2 nanocomposites (NCPs) is a serious scientific task because the synthesis of core/shell NCPs is more complex than the synthesis of individual NPs. The core/shell NCPs represent a multiphase nanomaterial that consists of an inner core coated with a shell of another type of material and therefore can combine various properties or even exhibit some new quality/activity/properties.[23] The development of core/shell NCPs based on the magnetic Fe_3O_4 NPs is not an entirely new direction, and various types of composites, where Fe_3O_4 NPs are coated with the organic or inorganic shell, have been studied, for example, as drug-delivery systems.[24] Apart from the enhancement of existing properties or the appearance of new ones, the presence of a shell around the magnetic Fe_3O_4 core can significantly increase their stability in suspensions, avoiding aggregation, protecting Fe_3O_4 against oxidation, and even raising the biocompatibility of the NPs.[24] The common chemical methods used for core/shell NCP fabrication are solvothermal methods, synthesis in aqueous systems (precipitation in solutions and a hydrothermal method), etc.[23] In most cases, Fe_3O_4/CeO_2 NCPs have been synthesized via the hydrothermal, sol−gel, or impregnation methods with further heating at temperatures over 300 °C.[25−28] However, the listed procedures are often unsuitable for biomedical applications due to the following reasons: (i) additional heat treatment can lead to enlargement of the NCP size, and the possibility of preparing a highly stable suspension based on them is a questionable task; (ii) the physicochemical properties of the obtained NCPs can be significantly changed, namely, the Ce^{3+} percentage on the CeO_2 surface after high-temperature exposure, which will result in the disappearance of their antioxidant potential. Moreover, in these works, primary attention was paid to functional studies of Fe_3O_4/CeO_2 NCPs without detailed physical−chemical characterization and assessment of the effect of the thickness of the outer layer around the magnetic core on the properties of composites. For example, Gao et al.[25] reported the fabrication of composites by the sol-precipitated method, but the study was mainly focused on the adsorption characteristics. Xu et al.[26] dealt with the Fe_3O_4/CeO_2 NCPs prepared by the impregnation method, but the key direction of their research was the investigation of the catalytic activity and the question of whether the obtained Fe_3O_4/CeO_2 is the structured NCP or just a simple mixture of two oxides was unanswered. It is noteworthy that detailed data on the structure of Fe_3O_4/CeO_2 composites promising for biomedical purposes are not very common in the literature, and only a few published articles are devoted to this task.[29−32] However, establishing the relationship between the structural and physical−chemical features of Fe_3O_4/CeO_2 NCPs and their biological activity is imperative for choosing the right approach to synthesis, which will allow one to obtain a composite with a complex "core/shell"-like structure.

In the present study, Fe_3O_4/CeO_2 NCPs were synthesized by the precipitation of CeO_2 NPs on the surface of previously obtained Fe_3O_4 NPs, and the resulting NCPs were investigated in detail for their physical−chemical, morphological, and magnetic properties. Considering the properties of pure Fe_3O_4 and CeO_2 NPs, it was also important to determine how the presence of CeO_2 in the outer layer of Fe_3O_4/CeO_2 affects the parameters of the magnetic inner core (Fe_3O_4) in the composite. Because both CeO_2 and Fe_3O_4 NPs are capable of affecting amyloidogenesis, it was expected that newly manufactured NCPs would also modulate and possibly enhance the inhibition/disassembly of protein aggregation. Therefore, the bioactivities of individual NPs and newly fabricated magnetic bimetal core/shell Fe_3O_4/CeO_2 NCPs were tested and compared *in vitro* as antiamyloidogenic and antioxidant activity.

2. MATERIALS AND METHODS

2.1. Materials. Iron(III) chloride hexahydrate ($FeCl_3·6H_2O$, 97%, CAS No. 10025-77-1), iron(II) sulfate heptahydrate ($FeSO_4·7H_2O$, 98%, CAS No. 7782-63-0), and cerium(III) acetylacetonate [Ce-

https://doi.org/10.1021/acsami.3c10845
ACS Appl. Mater. Interfaces 2023, 15, 49346−49361

$(acac)_3{\cdot}xH_2O$, CAS No. 206996-64-4] were obtained from Thermo-Fisher Scientific (Germany). An ammonia solution (NH_4OH, 25%) and ethanol (CH_3CH_2OH, 96%, CAS No. 64-17-5) were obtained from LLG Ukrorgsyntez (Ukraine). Insulin [human recombinant, expressed in yeast (E.C. 234-279-7, I2643, ~24 IU/mg protein)], 1-anilinonaphyhalene-8-sulfonic acid (ANS, A1028), hydrogen peroxide (H_2O_2, 95321), sodium chloride (NaCl, S3014), *N,N*-diethyl-*p*-phenylenediamine sulfate salt (DPD, ≥98%, 07672), Thioflavin T (ThT, T3516), and superoxide dismutase (SOD) determination kit (19160) were purchased from Sigma-Aldrich, Inc. (USA). All other chemicals were of reagent/analytical grade and were used without further purification.

2.2. Synthesis of Fe_3O_4/CeO_2 NCPs. *2.2.1. Synthesis of Fe_3O_4 NPs.* Fe_3O_4 NPs with spinel structure were synthesized via the cryochemical method by the well-known procedure described previously.[33] Briefly, an aqueous solution of $FeCl_3$ and $FeSO_4$ with a molar ratio of Fe^{2+}:Fe^{3+} = 1:2 was prepared and frozen using liquid nitrogen. The resulting frozen solution was placed in a 1 M solution of ammonium under constant stirring, observing the formation of a black precipitate. When the ice was completely melted, the reaction mixture was stirred for another 20 min on a mechanical stirrer. The produced Fe_3O_4 NPs were separated using a magnet, washed with the bidistilled water several times, and further dispersed in the measured volume of bidistilled water.

2.2.2. Synthesis of Fe_3O_4/CeO_2 NCPs. Fe_3O_4/CeO_2 "core/shell"-like NCPs were synthesized by the precipitation of the theoretically calculated "shell" of CeO_2 on the surface of previously synthesized magnetic Fe_3O_4 NPs. The amount of CeO_2 that was necessary for synthesis was determined by the calculation of the theoretical thickness of the CeO_2 "shell" around magnetic Fe_3O_4 NPs using the equations described in ref 34. Briefly, the volume of the "shell" for one "core/shell"-like NP was determined using formula (1) assuming that the NPs are spherical:

$$V = \frac{4\pi(R_1^{\,3} - R_2^{\,3})}{3} \quad (1)$$

where R_1 and R_2 are the radii of the coated and initial core NPs, respectively. Further, the mass of CeO_2 per one core/shell particle was calculated according to formula (2):

$$m = \rho V \quad (2)$$

where ρ is the density of CeO_2. Knowing the ratio of m_{shell} to m_{core}, it is possible to calculate the necessary mass of the shell for obtaining a certain amount of "core/shell" NPs.[34]

To fabricate a set of Fe_3O_4/CeO_2 "core/shell"-like NCPs, $Ce(AcAc)_3{\cdot}xH_2O$ [$Ce(AcAc)_3$ = cerium(III) 2,4-pentadionate] was used as the starting reagent. The synthesis of NCPs was performed according to the following procedure: 10 mL of a Fe_3O_4 suspension in a concentration of 25 mg/mL was added to 50 mL of the concentrated ammonia solution for functionalization of the NP's surface with −OH groups and left at constant stirring for 24 h at room temperature. The functionalized Fe_3O_4 NPs were separated on the magnet. An amount of 1.63, 3.43, or 5.84 g of $Ce(AcAc)_3$ was dissolved in 200 mL of ethanol to further obtain three samples of Fe_3O_4/CeO_2 NCPs with theoretically calculated values of the "shell" thickness. When $Ce(AcAc)_3{\cdot}xH_2O$ was completely dissolved, Fe_3O_4 NPs were added to the obtained solution in an ultrasound bath for 30 min. Further, the 1 M solution of ammonium was added dropwise to the suspension in the water bath (t ~ 55−60 °C). The obtained reaction mixture was stirred for 2 h at 60 °C. The fabricated NCPs were separated using the magnet with further centrifugation and washing with ethanol and bidistilled water. Finally, purified Fe_3O_4/CeO_2 NCPs were dispersed in the measured volume of bidistilled water.

2.3. X-ray Diffraction (XRD) Studies. XRD measurements for individual Fe_3O_4, CeO_2 NPs, and Fe_3O_4/CeO_2 NCPs were performed on a DRON-4 diffractometer using Cu Kα irradiation (nickel filter). A thin layer of each sample was deposited onto the quartz cuvette, and each XRD pattern was recorded in the range of 2θ = 20−90° with a step of 2θ = 0.04°. The time of exposition at each point was 8 s. The crystalline diameter of the NPs was estimated using the parameters of the peaks according to the Sherrer equation, as described in ref 35. The degree of crystallinity, which defines the percentage of the crystalline phase in the NPs sample, for both the individual NPs and their NCPs was calculated as a ratio of the total area of the crystalline peaks to the area of the whole XRD pattern using the approaches described in ref 36. The XRD pattern parameters were computed using the *Origin Pro 9.0* software package.

2.4. X-ray Photoelectron Spectroscopy (XPS). The surface chemical composition and chemical states of the samples were analyzed by utilizing XPS with a 1253.6 eV Mg Kα source with a total energy resolution of 0.8 eV. The spectra were treated by *KolXPD* software using the Shirley background and G*L or Voigt profile for fitting the spectra. The charging was corrected according to the C 1s reference corresponding to adventitious carbon (284.8 eV).

2.5. Transmission Electron Microscopy (TEM). Structural characterization of the samples was carried out using a probe-corrected JEM ARM200F analytical electron microscope (JEOL Ltd., Japan) operated at a 200 kV acceleration voltage. It was equipped with a Gatan Quantum SE (Gatan GmbH, Germany) for electron energy loss spectroscopy (EELS) measurements. For the acquisition of chemical maps by EELS spectral imaging in scanning TEM (STEM) mode, images were recorded using a high-angle annular dark field (HAADF) detector. For the spectral imaging experiment, the electron beam was scanned inside the designed area of interest (green rectangle labeled Spectrum imaging in HAADF-STEM images). The probe dwell time was set at 0.1 s per pixel. The chosen convergence angle was 14 mrad using a condenser aperture of 30 μm diameter, while the collection angle was 10 mrad at a 3 cm camera length and for a spectrometer entrance aperture of 5 mm. To image and process the spectral data, specialized routines under a Gatan digital micrograph were used. The samples in the suspension were diluted with distilled water and sonicated for 5 min to disperse the NPs. A drop of 5 μL from each dilution was deposited on a copper grid with a lacey carbon support film.

2.6. Dynamic Light Scattering (DLS). The hydrodynamic diameter (D_H) of individual Fe_3O_4 and CeO_2 NPs, as well as Fe_3O_4/CeO_2 NCPs, was investigated by DLS. The stability of the synthesized nanomaterials in the aqueous suspension was estimated by measuring the ζ-potential values. Synthesized NPs were dispersed in bidistilled water under ultrasound for 5 min (Elmasonic S30H, Germany). All measurements were performed in 1 mL of an aliquot at a concentration of approximately 15 μg/mL on a Litesizer 500 photon correlation spectroscopy system (Anton Paar GmBH, Austria) equipped with a semiconductor laser (40 mW, λ = 658 nm). The temperature during all measurements was 20 ± 1 °C. Measurements were performed in triplicate for all NPs and NCPs.

2.7. Magnetic Measurements. A vibrating-sample magnetometer (VSM) installed on a cryogen-free superconducting magnet (Cryogenic Ltd., U.K.) was employed to measure the magnetic moment of the studied samples. To obtain a true magnetic response of the "core/shell"-like NPs (without a diamagnetic contribution of the liquid carrier), the suspensions were lyophilized for 24 h. Then, the dry powders of known mass were encapsulated in a gelatin capsule and attached to a vibrating rod of the VSM. In this way, the magnetic moment of the powder was measured at room temperature (25 °C) and a magnetic field of up to 3 T.

2.8. Heating Efficiency Measurements. The heating efficiencies of Fe_3O_4/CeO_2 NCPs and individual NPs were estimated via measurements of their heating temperatures in an AMF. An aqueous suspension of each sample at a concentration of 20 mg/mL was placed in a magnetic coil of the AMF generator. The heating temperature for each sample was measured dynamically under the action of an AMF (H = 8.3°kA/m; f = 300°kHz) using the fiberoptic temperature sensor OPTOCON (Weidman, Germany). The specific loss power (SLP) value, which is the numerical scale for the heating efficiency of NPs, was calculated as described in ref 37 using formula (3):

https://doi.org/10.1021/acsami.3c10845
ACS Appl. Mater. Interfaces 2023, 15, 49346−49361

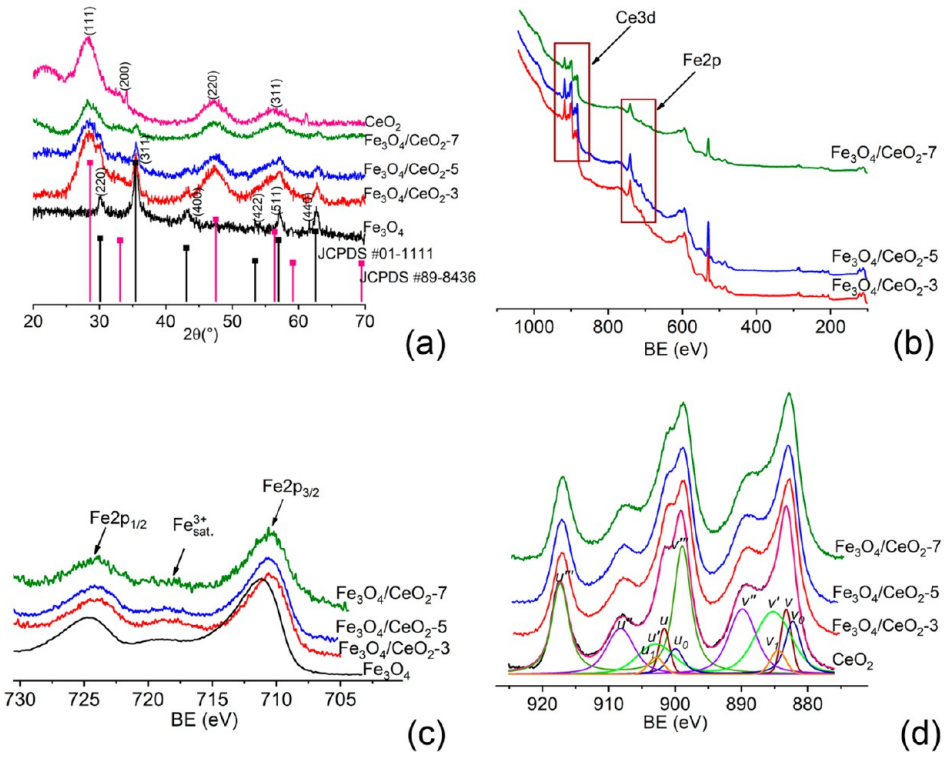

Figure 1. XRD and XPS data for Fe_3O_4/CeO_2 NCPs: (a) XRD patterns for pure Fe_3O_4, CeO_2 NPs, and Fe_3O_4/CeO_2 "core/shell"-like NCPs. (b) XPS survey spectra for NCPs. (c) Fe 2p XPS spectra for Fe_3O_4/CeO_2 NCPs and individual Fe_3O_4 NPs. (d) Ce 3d XPS spectra for Fe_3O_4/CeO_2 NCPs and individual CeO_2.

$$\mathrm{SLP} = \frac{CV_S}{m_{NPs}} \frac{dT}{d\tau} \tag{3}$$

where $dT/d\tau$ is the initial slope of the curves "T_h versus τ", C is the specific heat capacity of the solvent, V_S is the volume of the measured suspension, and m_{NPs} is the mass of the nanomaterial in the suspension.

2.9. Antiamyloidogenic Activity of Fe_3O_4/CeO_2 NCPs on Insulin Amyloid Fibrillization Examined Using ThT Fluorescence and Atomic Force Microscopy (AFM). To elucidate the antiamyloidogenic potential of core/shell NCPs, dose- and time-dependent experiments were performed. Within both dose- and time-dependent measurements, insulin was dissolved in a 100 mM NaCl solution, pH 1.6 (hereinafter referred to as NaCl solution), to obtain a final concentration of 0.145 μg/mL, which corresponds to 25 μM, and the solution was incubated in an Eppendorf comfort thermomixer at 65 °C for 2 h under constant agitation (500 rpm). For disassembly experiments, a stock solution of 2 mg/mL (344 μM) insulin fibrils in NaCl solution was prepared. The presence of insulin amyloid fibrils was monitored by ThT fluorescence assay, and the morphology of the insulin amyloid fibrils was evaluated by AFM.

For the dose-dependent inhibition analysis, aliquots of Fe_3O_4/CeO_2 NCPs (from freshly prepared stock solutions in water) were added to 25 μM insulin in NaCl solution with a protein-to-NPs ratio ranging from 1:0.025 to 1:15 (w/w), followed by incubation under the conditions described above. Disassembly measurements were performed by the incubation of 25 μM preformed insulin fibrils in the presence of Fe_3O_4/CeO_2 NCPs (ratio 1:0.025−1:15) for 24 h at 37 °C. The pH of the buffers in the inhibition and disassembly experiments did not change upon the addition of NPs. Within the kinetic-dependent inhibition analysis, aliquots of the control and Fe_3O_4/CeO_2 NCPs-containing samples were withdrawn at various times and analyzed by ThT assay. The extent of inhibition and disassembly activity was assessed by ThT fluorescence assay. ThT was added to the studied samples at a final protein-to-ThT concentration ratio of 1:5, and after 1 h of incubation in the dark at 37 °C, the fluorescence intensity was measured using a 96-well plate by a Synergy MX (BioTek) spectrofluorometer. The formation of insulin amyloid fibrils was also monitored by the fluorescence of ANS, as described recently.[18] The experimental data were fitted by a four-parameter sigmoidal logistic equation using *SigmaPlot*, version 14.0 (Systat Software Inc.). The error bars represent the average deviation for the repeated measurements of five separate samples. The experimental approach was described previously by Siposova et al.[17,18,38]

Samples for AFM visualization were prepared by spotting 10 μL of sample solutions on a freshly cleaved mica surface. After 5 min of adsorption, the samples were washed with ultrapure water and gently dried under a soft stream of purified nitrogen gas. AFM imaging was performed on a scanning probe microscope (Veeco di Innova, Bruker AXS Inc., Madison, WI) working in tapping mode as described previously.[17,18,38] The presented images were made by using NanoScope Analysis 1.20 without additional modifications. All AFM experiments were performed at 25 ± 1 °C.

2.10. Examination of the Pseudoenzymatic Activity. The catalase-like activity of the studied Fe_3O_4/CeO_2 NCPs was examined using a colorimetric method based on the oxidation of DPD.[38] A detailed experimental approach for NCPs was described recently.[22] The reaction was always initiated by the addition of NPs to a final concentration of 10 μg/mL. The kinetics of H_2O_2 decomposition was monitored at 551 nm at 25 °C using a 96-well plate by a Synergy MX (BioTek) spectrofluorometer. The oxidase-like activity of CeO_2 NPs was monitored in the absence of H_2O_2.

The pseudo-SOD activity of CeO_2 NPs was assessed by a colorimetric assay using a commercial SOD kit that utilizes 2-(4-iodophenyl)-3-(4-nitrophenyl)-5-(2,4-disulfophenyl)-2*H*-tetrazolium monosodium salt (WST-1), which produces the water-soluble formazan dye upon reduction by a superoxide anion. Measurements were performed in a 96-well plate at a final particle concentration of 75 μg/mL using a microplate reader (Synergy BioTek). SOD-like activity, expressed as A_{SOD} (inhibition rate, %), was defined as the percentage of dismutation of superoxide radicals.[18,22]

https://doi.org/10.1021/acsami.3c10845
ACS Appl. Mater. Interfaces 2023, 15, 49346−49361

3. RESULTS AND DISCUSSION

3.1. Preparation and Characterization of Fe_3O_4/CeO_2 NCPs. A set of Fe_3O_4/CeO_2 NCPs was synthesized by the precipitation of CeO_2 NPs on the surface of previously fabricated Fe_3O_4 NPs via the cryochemical method. To evaluate the size of the CeO_2 NPs, which will be further used for "shell" deposition, pure CeO_2 NPs were obtained via precipitation using $Ce(AcAc)_3$ as the starting reagent. When $Ce(AcAc)_3$ was dissolved in an alcohol solution with further addition of an aqueous ammonia solution (pH ∼ 9), $Ce(AcAc)_3$ hydrolyzed, and CeO_2 NPs were finally formed, which was confirmed by the XRD and HRTEM data described below.

Figure 1a presents the XRD patterns for Fe_3O_4/CeO_2 NCPs as well as pure Fe_3O_4 and CeO_2 NPs for comparison. Fe_3O_4 NPs display six peaks in the XRD pattern marked with (*hkl*) indexes, which are consistent with the International Database (JCPDS Card No. 01-1111), which verifies the formation of single-phase NPs with spinel structure (space group *Fd*3*m*). The crystalline diameter of NPs was calculated by Sherrer's equation using the parameters of the (*311*) peak, and it was found to be 12.8 nm. The degree of crystallinity for Fe_3O_4 NPs, which was computed as a ratio of the crystalline peak area to the area of the whole pattern, equals 40.3%. Individual CeO_2 NPs have four visible peaks in the XRD pattern indexed to the (*111*), (*200*), (*220*), and (*311*) atomic planes for the cubic fluorite structure of CeO_2 with the space group *Fm*3*m* (JCPDS Card No. 89-8436). The significant peak broadening in the XRD pattern of CeO_2 can indicate the formation of ultrasmall NPs,[39] and it is evidenced by the calculations via Sherrer's formula, using the parameters of the (*111*) peak: the crystalline diameter of individual CeO_2 NPs equals 2.9 nm. The degree of crystallinity for these NPs was found to be 21%. The evaluated values of the crystalline diameters for individual Fe_3O_4 and CeO_2 NPs were considered for calculating the "theoretical" shell thickness in the NCPs of Fe_3O_4/CeO_2 using the formulas described in the Materials and Methods section. Three samples of Fe_3O_4/CeO_2 with calculated shell thicknesses of 3, 5, and 7 nm were obtained. Hereinafter, these samples are marked as **Fe_3O_4/CeO_2-3**, **Fe_3O_4/CeO_2-5**, and **Fe_3O_4/CeO_2-7**, respectively.

XRD patterns of Fe_3O_4/CeO_2 NCPs (Figure 1a) reveal the superposition of peaks from Fe_3O_4 and CeO_2 NPs, suggesting the coexistence of both phases in the NCPs. The asymmetry of peaks at $2\theta = 28.4°$, 47.6°, and 57.2° indicates the overlapping peaks of Fe_3O_4 and CeO_2 compared with their positions in the XRD patterns of individual NPs, and it becomes less visible with an increase of CeO_2 in Fe_3O_4/CeO_2 NCPs. The Fe_3O_4 peak (*311*) at 35.5° in the NCPs is not shifted relative to its position in the XRD pattern of bare Fe_3O_4 NPs, suggesting that any complex chemical interactions between the two types of oxide NPs are absent in the composite. The intensity of the (*311*) peak decreases with the growth of the CeO_2 percentage in the sample, which can point to covering the magnetic Fe_3O_4 NPs with the CeO_2 "shell". The degree of crystallinity for the obtained Fe_3O_4/CeO_2 NCPs reveals the following tendency: it equals 40.2% for **Fe_3O_4/CeO_2-3** NCPs, but for **Fe_3O_4/CeO_2-5** and **Fe_3O_4/CeO_2- 7** NCPs, it sharply reduces to 25.3 and 22.3%, respectively. When these data are compared with the values for individual NPs, it can be concluded that the degree of crystallinity for Fe_3O_4/CeO_2 NCPs approaches the degree of crystallinity of individual CeO_2 NPs with an increase in the CeO_2 content in the NCP. These data suggest the existence of CeO_2 around the Fe_3O_4 NPs, and its amount grows from **Fe_3O_4/CeO_2-3** to **Fe_3O_4/CeO_2-7** NCPs.

The chemical state of the surface of the fabricated Fe_3O_4/CeO_2 NCPs was studied in detail by the XPS method. The XPS spectra for individual Fe_3O_4 and CeO_2 NPs were recorded for comparison. The presence of Fe 2p and Ce 3d peaks in the XPS spectra of NCPs indicates the coexistence of both oxides in the NCPs (Figure 1b). Each spectrum also displays C 1s and O 1s peaks. The areas of all presented peaks were determined after subtracting the Shirley background to evaluate semi-quantitatively the Ce/Fe atomic ratio on the NP's surface. The atomic percentages of Fe and Ce were calculated according to formula (4):[40]

$$w_{at.} = \frac{I_x/S_x}{\sum I_x/S_x} \quad (4)$$

where I_x is the area of the XPS peak of an element and S_x is the atomic sensitivity factor.

The atomic sensitivity factors equal 8.808 for Ce 3d, 2.957 for Fe 2p, 0.711 for O 1s, and 0.296 for C 1s. The calculated $w_{at.}(Ce)/w_{at.}(Fe)$ atomic ratios are listed in Table 1, and they are used as a basis for further discussions. The obtained results reveal that the $w_{at.}(Ce)/w_{at.}(Fe)$ atomic ratio grows with increasing CeO_2 content in the Fe_3O_4/CeO_2 NCPs. Such a dependence can indicate the coating of Fe_3O_4 NPs with a CeO_2 "shell"; however, such a "shell" around the magnetic NPs can be nonuniform. Therefore, this assumption must be supported by other methods such as HRTEM.

Table 1. Semiquantitative XPS Data for Fe_3O_4/CeO_2 NCPs[a]

sample	$w_{at.}(Ce)/w_{at.}(Fe)$	$w_{at.}(Fe^{3+})/w_{at.}(Fe^{2+})$	$w_{at.}(Ce^{3+})/w_{at.}(Ce^{4+})$
Fe_3O_4 NPs		2.11	
Fe_3O_4/CeO_2-3	7.75	2.07	0.35
Fe_3O_4/CeO_2-5	7.98	2.05	0.37
Fe_3O_4/CeO_2-7	9.17	1.97	0.49
CeO_2 NPs			0.49

[a] $w_{at.}$ = atomic percent (%).

Both the Fe 2p and Ce 3d spectra shown in parts c and d of Figure 1, respectively, were analyzed in detail for a deeper evaluation of the chemical states of Fe and Ce ions in the NCPs. In general, XPS Fe 2p spectra exhibit a combination of two main peaks, which correspond to the Fe $2p_{3/2}$ and Fe $2p_{1/2}$ sublevels, respectively (Figure 1c), and these data are in good agreement with the known literature.[41] Additionally, the Fe 2p spectra have a visible peak at approximately 719.4 eV, which can be classified as a Fe^{3+} satellite peak and usually presents in the XPS spectra of Fe_2O_3 or α-FeOOH.[42] The appearance of this peak in the XPS spectra of bare Fe_3O_4 NPs suggests the partial oxidation of naked Fe_3O_4, which is well-known by its instability in air, or the formation of an intermediate α-FeOOH phase during the synthesis of Fe_3O_4 at low temperature.[43,44] When the Fe 2p spectra of the NCPs are compared with the spectrum of an individual Fe_3O_4, it can be observed that the peak at binding energy (BE) = 719.4 eV becomes less visible with the growth of the CeO_2 percentage in the NCP. This suggests that the presence of CeO_2 provides the protection of Fe_3O_4 from oxidation, which leads to the higher stability of Fe_3O_4. Figure 1c also shows that the peaks in the Fe 2p spectra of Fe_3O_4/CeO_2 NCPs are slightly shifted to the lowest values

https://doi.org/10.1021/acsami.3c10845
ACS Appl. Mater. Interfaces 2023, 15, 49346−49361

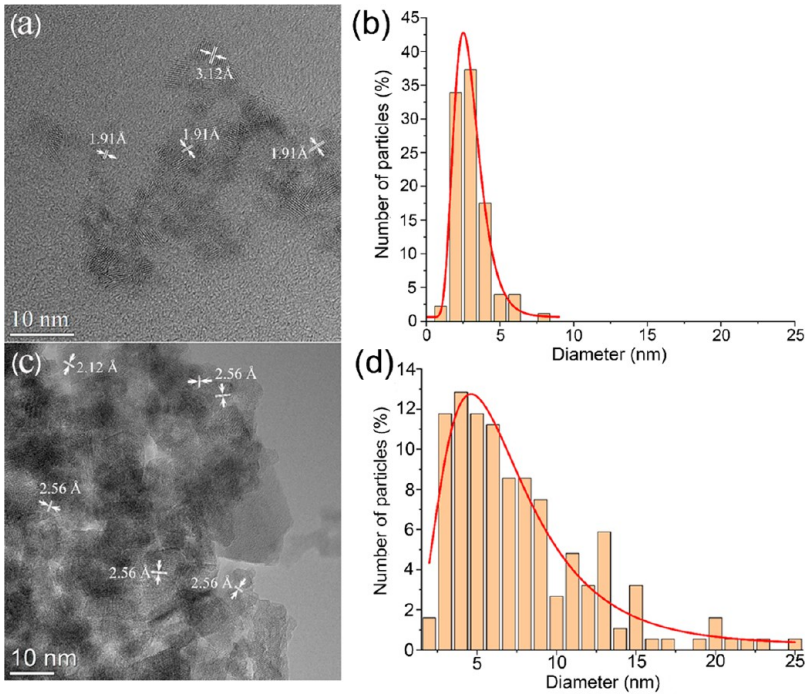

Figure 2. HRTEM image of individual CeO_2 NPs obtained from $Ce(AcAc)_3$ (a) and their particle size distribution (b). HRTEM image of individual Fe_3O_4 NPs (c) and their particle size distribution (d).

of the BEs compared to the spectrum of an individual Fe_3O_4, which can be caused by weak intramolecular interactions between Fe_3O_4 and CeO_2, as well as a decrease in the oxidative state of the Fe ion from Fe^{3+} to Fe^{2+}.[45]

Clarifying the impact of CeO_2 NPs at the surface of magnetic Fe_3O_4 NPs on the chemical state of Fe ions requires one to perform an additional fitting of the Fe 2p spectrum for an approximate semiquantitative estimation of the $w_{at.}(Fe^{3+})/w_{at.}(Fe^{2+})$ ratio. Only the Fe $2p_{3/2}$ peak is usually used for the semiquantitative determination of the Fe^{2+} and Fe^{3+} percentages. Fitting of the Fe 2p spectra is rather complicated, although the main principles are well described.[46,47] However, there are many works in which this procedure is simplified, and the Fe $2p_{3/2}$ peak is considered to be a combination of three main peaks, which correspond to three positions of Fe ions in the spine structure: Fe^{2+} in the octahedral positions (BE = 709.8 ± 0.2 eV), Fe^{3+} in the octahedral positions (BE = 710.5 ± 0.2 eV), and Fe^{3+} in the tetrahedral positions (BE = 711.9 ± 0.2 eV).[41,48] To evaluate semiquantitatively the Fe^{3+}/Fe^{2+} ratio within the present study, these simplified assumptions were used. The calculated $w_{at.}(Fe^{3+})/w_{at.}(Fe^{2+})$ atomic ratios are summarized in Table 1. The obtained data reveal that the $w_{at.}(Fe^{3+})/w_{at.}(Fe^{2+})$ ratio for individual Fe_3O_4 NPs is 2.11, which is higher than the stoichiometrically expected value $[w_{at.}(Fe^{3+})/w_{at.}(Fe^{2+}) = 2.00]$. It can indicate the partial oxidation of Fe_3O_4 NPs in air or the formation of the impurity phase of α-FeOOH during the synthesis, which leads to an increase in the Fe^{3+} percentage. During the transition to Fe_3O_4/CeO_2 NCPs, the $w_{at.}(Fe^{3+})/w_{at.}(Fe^{2+})$ ratio on the surface of NPs tends to reduce; i.e., the percentage of Fe^{2+} increases with growth of the CeO_2 "shell" around Fe_3O_4 NPs. The semiquantitative evaluation of the $w_{at.}(Fe^{3+})/w_{at.}(Fe^{2+})$ ratio in the samples is in good correlation with the qualitative analysis of the XPS Fe 2p spectra. Fe_3O_4/CeO_2 NCPs include two Ox−Red ion couples: Fe^{3+}/Fe^{2+} and Ce^{3+}/Ce^{4+}. The evaluations of the XPS data for the NCPs described above suggest that the appearance of CeO_2 around Fe_3O_4 NPs assists in the disappearance of the impurity phase of α-FeOOH by promoting the partial reduction of Fe^{3+} to Fe^{2+} ions, and its complete conversion to Fe_3O_4 also provides some protection of the surface of magnetic NPs against their oxidation in air.

To estimate the chemical state of Ce ions and evaluate the $w_{at.}(Ce^{3+})/w_{at.}(Ce^{4+})$ ratio on the surface of composite NPs, all XPS Ce 3d spectra were fitted following the well-described procedure.[22,49] The XPS Ce 3d spectrum was resolved to five peaks, which correspond to the Ce $3d_{5/2}$ and Ce $3d_{3/2}$ sublevels (Figure 1d). The peak located at BE = 916.9 ± 0.1 eV is a clear indicator of Ce^{4+} ions. The spectra show the coexistence of Ce^{3+} and Ce^{4+} ions. The XPS Ce 3d spectra can be well fitted with five main doublets: doublets labeled with v_0-u_0 and $v'-u'$ correspond to Ce^{3+} ions, and doublets labeled with v−u, v″−u″, and v‴−u‴ correspond to Ce^{4+} ions.[50] Previously it was explained that the peak corresponding to Ce^{4+} at the lowest BE is asymmetrical; therefore, the doublet v−u is considered to be the sum of two doublets v−u and v_1-u_1 for better fitting of the spectra.[22] The percentage of Ce^{3+} ions in each sample was determined to be the ratio of the peak areas of Ce^{3+} doublets to the total area of all doublets as described in refs 22 and 51, and the calculated values are listed in Table 1. It is noticeable that the sizes of the CeO_2 particles remained at the same level when a set of Fe_3O_4/CeO_2 NCPs were synthesized; therefore, the $w_{at.}(Ce^{3+})/w_{at.}(Ce^{4+})$ ratio was expected to be similar for all samples. However, the evaluated data showed the following dependence: the $w_{at.}(Ce^{3+})/w_{at.}(Ce^{4+})$ ratio on the NCP's surface was slightly reduced for the **Fe_3O_4/CeO_2-3** and **Fe_3O_4/CeO_2-5** samples compared to the value for individual CeO_2 NPs. This correlates well with the previous semiquantitative evaluations of $w_{at.}(Fe^{3+})/w_{at.}(Fe^{2+})$ ratios and can be connected with Ox−Red processes between Fe and Ce ions: the Ce^{3+} ion percentage decreases simultaneously with a decrease of the Fe^{3+} ion percentage. In the case of the **Fe_3O_4/CeO_2-7** sample, the total percentage of

https://doi.org/10.1021/acsami.3c10845
ACS Appl. Mater. Interfaces 2023, 15, 49346−49361

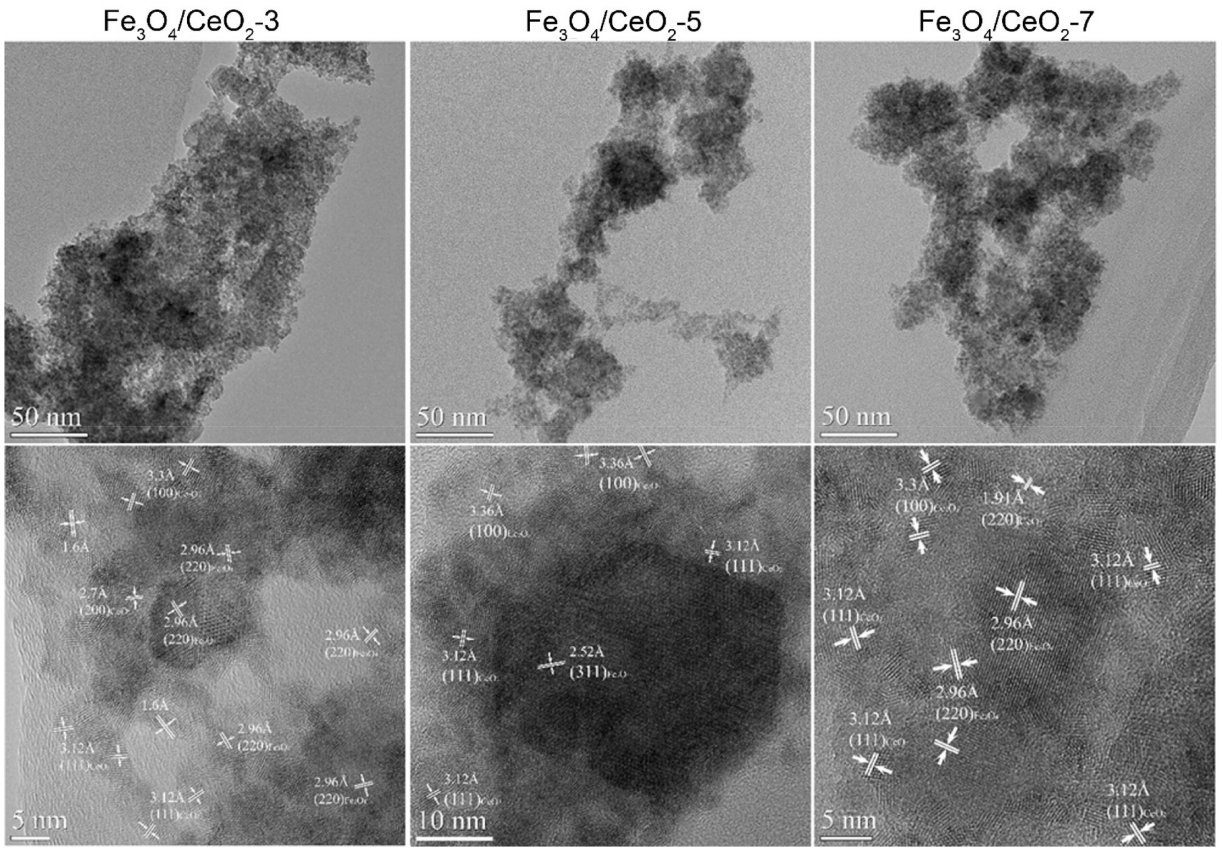

Figure 3. TEM (upper row) and HRTEM (bottom row) images of **Fe_3O_4/CeO_2-3**, **Fe_3O_4/CeO_2-5**, and **Fe_3O_4/CeO_2-7** NCPs.

Fe ions at the surface was negligible and the $w_{at.}(Ce^{3+})/w_{at.}(Ce^{4+})$ ratio was evaluated to be the same as that for the individual CeO_2 NPs.

Figure 2 shows the morphological characteristics of the individual CeO_2 and Fe_3O_4 NPs. The high-resolution TEM (HRTEM) image of the synthesized CeO_2 NPs (Figure 2a) demonstrates that NPs are ultrafine and nonagglomerated with an average size of 3−3.5 nm and a narrow size distribution. The lattice fringes are characteristic of CeO_2 crystallized in a cubic structure with the space group $Fm\bar{3}m$, and the lattice parameters $a = b = c = 5.4124(1)$ Å can be observed in the HRTEM image: 3.12 Å for the (111) plane and 1.91 Å for the (220) plane. The HRTEM image of the individual Fe_3O_4 NPs (Figure 2c) demonstrated the formation of spherical and faceted NPs. Spherical NPs have an average size of 5.0 nm, while faceted NPs are 10.2 nm. In the HRTEM image (Figure 2c), the lattice fringes are characteristic of magnetite crystallized in a cubic structure with the space group $Fd\bar{3}m$, and the lattice parameters $a = b = c = 8.491(3)$ Å can be clearly observed: 2.56 Å for the (311) plane, 2.45 Å for the (222) plane, and 2.12 Å for the (400) plane. The obtained results for individual NPs correlate well with the XRD data.

Detailed HRTEM investigations were performed to study the morphologies of the synthesized Fe_3O_4/CeO_2 NCPs. Their representative HRTEM images are shown in Figure 3. The obtained HRTEM data reveal that Fe_3O_4 NPs are surrounded by ultrafine CeO_2 NPs. For Fe_3O_4 NPs, the predominants are the lattice fringes of 2.96 Å that correspond to the (*220*) plane and of 2.52 Å that correspond to the (*311*) plane of the cubic spinel structure. At the same time, the lattice fringes of 3.12 are predominant for CeO_2 NPs, which correspond to the (*111*) plane of the cubic fluorite structure. However, one can observe the presence of CeO_2 NPs with lattice fringes of 3.30 Å, which correspond to the (*100*) plane of the hexagonal structure typical for cerium(III) oxide. Theoretically, such a regularity can be explained in the following way. As we have shown previously,[22] the nanoscale CeO_2 contains Ce^{3+} ions on their surfaces, and their percentage on the surface of NPs grows with the decreasing of the particle's size. Moreover, the literature data indicate that the critical diameter for CeO_2 NPs, under which all Ce^{4+} ions switch to Ce^{3+}, is 1.9 nm. CeO_2 NPs in the NCPs have an average particle size of 3−3.5 nm; however, their size distribution varies from 1.5 to 5.0 nm (Figure 2b). Therefore, it can be assumed that NPs with sizes of 1.5−2 nm completely switch to Ce_2O_3 with a hexagonal structure.

The surrounding of Fe_3O_4 NPs by CeO_2 NPs was also confirmed by EELS analysis, for which representative maps of the elemental distribution are shown in Figure 4a−c. The elemental maps that correspond to the Fe $L_{2,3}$-edge at 708−721 eV and the Ce $M_{4,5}$-edge at 880−898 eV were extracted after removal of the background using the power-law background model. For comparison, Figure 4d represents the data of the elemental analysis for the mechanical mixture, which contained Fe_3O_4 and CeO_2 in the ratio as calculated for the synthesis of **Fe_3O_4/CeO_2-5** NCPs. It is observed in Figure 4d that, in the case of a simple mixture formation between Fe_3O_4 and CeO_2, there are large areas enriched with Fe_3O_4 and CeO_2, *and* both phases are completely separated in the sample. Analysis of the spatial distributions of Fe and Ce in the Fe_3O_4/CeO_2 samples reveals that the Fe_3O_4 NPs are neatly surrounded by CeO_2 NPs. However, such a CeO_2 "shell" is not entirely uniform. This uniformity can be explained by the

https://doi.org/10.1021/acsami.3c10845
ACS Appl. Mater. Interfaces 2023, 15, 49346−49361

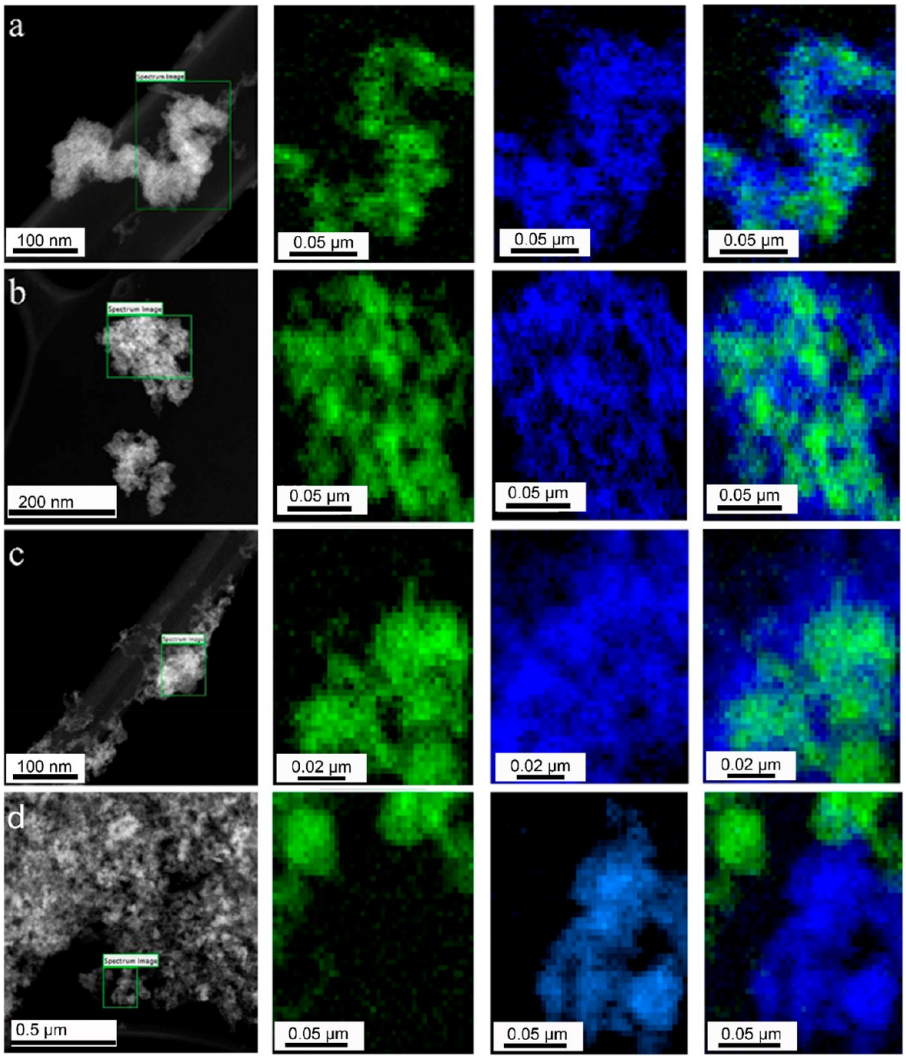

Figure 4. HAADF-STEM image with a green rectangle showing the area in which the spectral image was acquired, maps of the elemental distribution for Fe (green) and Ce (blue), and overlay of maps for **Fe_3O_4/CeO_2-3** (a), **Fe_3O_4/CeO_2-5** (b), **Fe_3O_4/CeO_2-7** (c), and a mechanical mixture (d).

Table 2. DLS Data for Fe_3O_4/CeO_2 NCPs Dispersed in Bidistilled Water

sample	D_H(intensity) (nm)	PdI	ζ potential (mV)	initial pH of the suspension
Fe_3O_4	243.2 ± 14.2	0.239 ± 0.014	+18.0 ± 0.6	6.0 ± 0.1
Fe_3O_4/CeO_2-3	342.5 ± 12.3	0.244 ± 0.016	+23.0 ± 1.2	5.2 ± 0.1
Fe_3O_4/CeO_2-5	423.9 ± 8.53	0.183 ± 0.018	+34.0 ± 0.6	4.8 ± 0.1
Fe_3O_4/CeO_2-7	458.7 ± 30.1	0.291 ± 0.018	+37.1 ± 0.8	4.7 ± 0.1
CeO_2	229.41 ± 27.5	0.122 ± 0.016	+42.0 ± 0.7	4.1 ± 0.1

fact that calculations of the "shell" thickness are completely theoretical and do not allow one to take into account the particle size distribution for both oxides. However, complex HRTEM and EELS data allow one to assume the formation of Fe_3O_4/CeO_2 with a so-called "core/shell"-like structure; similar data were found in the literature for other types of inorganic composites based on CeO_2.[52]

The properties of the fabricated Fe_3O_4/CeO_2 NCPs in their aqueous suspensions were analyzed by DLS, and the main parameters are summarized in Table 2. The hydrodynamic diameter of individual Fe_3O_4 NPs is much higher than the size determined by TEM. This was expected and can be explained for two reasons. First, DLS measures the size of colloidal NPs in the solutions; therefore, the diameter of the NPs is affected by the associated solvent molecules, while TEM allows one to analyze of the dry samples and calculate of the crystalline diameter of pure NPs.[53] Second, the bare magnetic Fe_3O_4 NPs tend to aggregate in the aqueous solutions due to the intramolecular interactions between NPs, such as van der Waals forces or magnetic interactions caused by the residual magnetization.[54] The various stabilizers, such as oleic acid, citric acid, or chitosan, are usually used to prevent the agglomeration of Fe_3O_4 NPs just after synthesis. In addition, these stabilizers protect the magnetic NPs from oxidation to γ-Fe_2O_3 in air.[55] DLS measurements have demonstrated that the coating of Fe_3O_4 NPs with CeO_2 leads to a significant increase in their hydrodynamic diameter: the larger amount of CeO_2 NPs surrounds the magnetic NPs; the higher hydrodynamic

https://doi.org/10.1021/acsami.3c10845
ACS Appl. Mater. Interfaces 2023, 15, 49346−49361

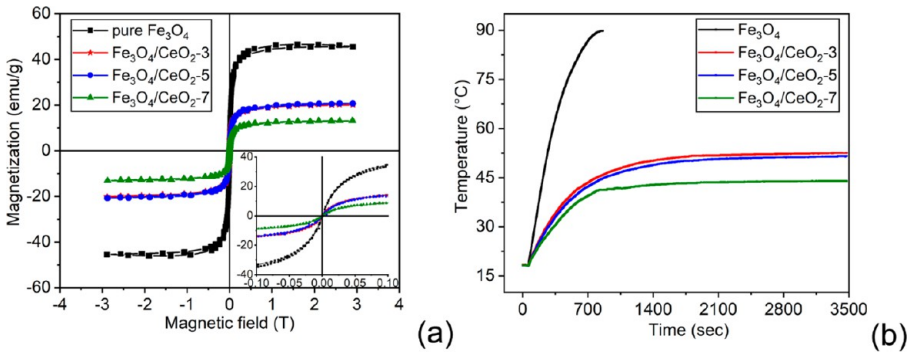

Figure 5. Hysteresis loops for Fe_3O_4/CeO_2 NCPs (a) and curves of heating temperature versus time of the AMF action on the magnetic fluids based on Fe_3O_4/CeO_2 NCPs (b).

diameter is observed for the obtained NCP (Table 2). It is noticeable that the polydispersity index (PdI) for all NCPs was less than 0.3, and this indicates the formation of relatively monodispersed NCPs. These data can additionally manifest the formation of composite "core/shell"-like Fe_3O_4/CeO_2 NPs but not just a simple mixture of two types of nanomaterials.

Table 2 represents the ζ-potential values for all synthesized NPs, which determine their stability in the aqueous suspensions; the initial pH for each suspension at which measurements were performed is also given in Table 2. The obtained data reveal that growth of the CeO_2 "shell" around the magnetic NPs results in an increase in the ζ potential for the resulting NCPs.

Fe_3O_4/CeO_2-5 and **Fe_3O_4/CeO_2-7** NCPs have ζ-potential values higher than +30 mV, which indicates the formation of highly stable water suspensions. Previously, we showed that CeO_2 NPs are self-stabilized in their aqueous suspensions due to the existence of hydrated Ce^{4+} ions on their surface,[22] and they form highly stable suspensions in bidistilled water without using any additional substances. At the same time, it is well-known that bare Fe_3O_4 NPs have hydroxyl (−OH) groups on their surfaces due to the chemisorption of water molecules in the solution. Some of these −OH groups are amphoteric; therefore, the surface charge significantly depends on the pH of the suspension.[54] Individual uncoated Fe_3O_4 NPs obtained by the cryochemical method exhibit pH values near 6.0 in the aqueous suspension and have ζ potential values of +18 mV, which is in good correlation with the data known in the literature and indicates low stability of such NPs in bidistilled water.[54] Such data are also in good correlation with the TEM results (Figure 2c), which demonstrate some agglomeration of pure Fe_3O_4 NPs. Before the Fe_3O_4@CeO_2 composites were fabricated, Fe_3O_4 NPs were additionally prefunctionalized with −OH groups in an ammonia solution. After this, their surface became negatively charged (ζ potential ∼ −11 mV), and the formation of the CeO_2 "shell" around magnetic NPs can be explained by the electrostatic interactions between negatively charged Fe_3O_4 NPs and positively charged CeO_2. The transfer to Fe_3O_4/CeO_2 NCPs shows some reduction in the pH values of the suspensions, together with an increase in their ζ-potential values (Table 2). These data suggest that CeO_2, which has an acidic pH in the aqueous suspensions,[22] forms a protective "shell" around the magnetic Fe_3O_4 NPs. Consequently, the CeO_2 "shell" can be considered to be a stabilizer of the magnetic Fe_3O_4 NPs against sedimentation in the obtained magnetic fluids.

Measurements of the magnetization of the obtained NCPs and individual Fe_3O_4 NPs were carried out at 25 °C to determine how the appearance of the CeO_2 "shell" around Fe_3O_4 NPs affects their magnetic properties. The character of the field dependences of magnetization for NPs indicates the ferromagnetic properties of the NCPs (Figure 5a). The magnetic parameters calculated from the measured curves are summarized in Table 3. The pure magnetite powder exhibits

Table 3. Magnetic Parameters of the Fe_3O_4/CeO_2 NCPs

sample	magnetization saturation (emu/g)	coercive force (mT)	SLP (W/g)
Fe_3O_4	46.6	9.4	38.8
Fe_3O_4/CeO_2-3	20.2	3.5	34.9
Fe_3O_4/CeO_2-5	20.7	1.9	29.7
Fe_3O_4/CeO_2-7	13.0	1.2	21.4

the highest saturation magnetization, reaching 46.6 emu/g. The composite Fe_3O_4/CeO_2 samples containing CeO_2 have remarkably lower magnetization of saturation values, and they tend to decrease with the growth of the CeO_2 content in the samples. Such results were expected and are caused by the appearance of nonmagnetic CeO_2 around the magnetic Fe_3O_4 NPs as well as by a decrease of the concentration of Fe_3O_4 in the same volume of the sample. The close values of magnetization of saturation for **Fe_3O_4/CeO_2-3** and **Fe_3O_4/CeO_2-5** NCPs can be related to the nonuniform surrounding of Fe_3O_4 NPs by the CeO_2 "shell", as evidenced by HRTEM. The inset to Figure 5a shows that each magnetization loop has negligible coercivity, implying a superparamagnetic state of the NPs' magnetic moments. The inset also reveals decreasing magnetic susceptibility (initial magnetization slope) in the low-field region with an increasing amount of CeO_2 in the sample.

The aqueous suspensions of synthesized Fe_3O_4/CeO_2 NCPs and individual NPs in a concentration of 20 mg/mL were exposed to AMF to determine their ability to heat up in AMF and estimate the impact of the outer layer of CeO_2 on the heating efficiency of NCPs. Figure 5b shows the dependence of the heating temperature of the NPs on the time of exposure to AMF for all NPs. The calculated SLP values are listed in Table 3. The obtained results reveal that the bare Fe_3O_4 NPs are uncontrollably heated to a high temperature, which is in good agreement with the literature data because Fe_3O_4 has a Curie temperature of approximately 585 °C.[56] It was observed that the presence of a CeO_2 "shell" decreases the heating ability of the Fe_3O_4/CeO_2 NCPs. The heating efficiency of the NCPs decreases with an increase in CeO_2 in the "shell" layer, which is

https://doi.org/10.1021/acsami.3c10845
ACS Appl. Mater. Interfaces 2023, 15, 49346−49361

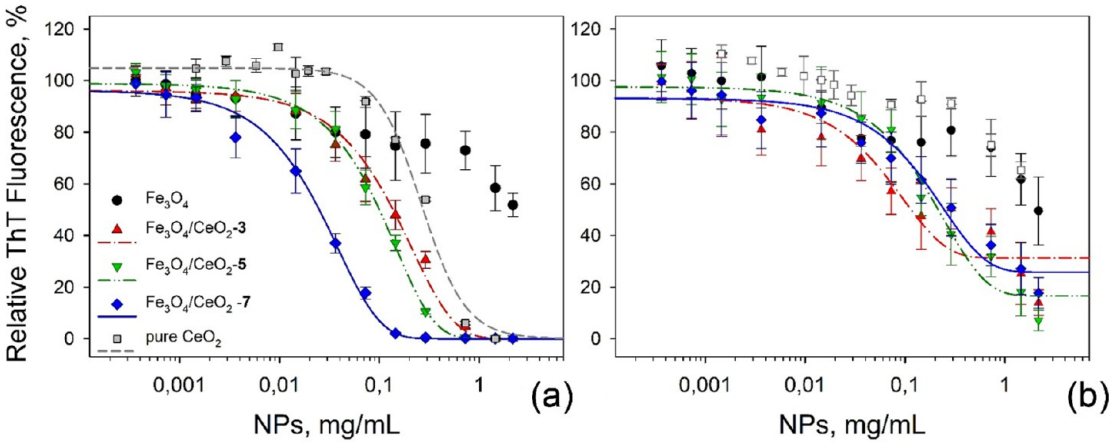

Figure 6. Evaluation of the antiamyloid activity of Fe_3O_4 and Fe_3O_4/CeO_2 NCPs. Dose-dependent quantification of the inhibition activity (a) and the disassembly of preformed fibrils (b) monitored by ThT fluorescence assay. The ThT fluorescence data were normalized to fluorescence intensities recorded after the complete fibrillization of insulin alone (taken as 100%). Each experiment was performed five times; error bars represent the average deviation for repeated measurements of five separate samples.

expressed as a decrease in the SLP values (Table 3). The results obtained correlate well with the magnetic measurements. Increasing the thickness of the outer layer of the CeO_2 "shell" in NCPs reduces the percentage of Fe_3O_4 in the same mass as NCPs used to prepare the suspension for measurements. In other words, the mass of the magnetic component that provides the heating ability in AMF decreases with an increase in the content of nonmagnetic CeO_2. Unlike bare Fe_3O_4 NPs, it can be seen that the heating temperature of Fe_3O_4/CeO_2 NCPs reaches its maximum value after some time of exposure to AMF, and the maximum heating temperature also decreases with an increase in the content of CeO_2 in the "shell". This effect is not associated with any changes in the Curie temperature values and can be explained by the simple heat transfer from the Fe_3O_4 NPs to the surrounding suspension. The obtained results show that the CeO_2 "shell" in Fe_3O_4/CeO_2 NCPs can also be used to reduce the maximum heating temperature of Fe_3O_4 NPs in AMF. This is a very encouraging result because changing the thickness of the CeO_2 "shell" around Fe_3O_4 NPs provides the possibility of fine-tuning the heating temperature of NCPs in the temperature range 42−50 °C, which is suitable for further biomedical purposes.

3.2. Evaluation of the Fe_3O_4/CeO_2 NCPs Bioactivity.

The bioactivity of newly fabricated magnetic bimetal core/shell Fe_3O_4/CeO_2 NCPs was tested *in vitro* as the antiamyloidogenic and antioxidant activity. Fabricated NCPs were assessed for their antiamyloidogenic potential using a well-known experimental approach based on inhibition and disaggregation analysis of the amyloid fibril formation of insulin.[12,17,18,57,58] The pseudoenzymatic antioxidant activities were evaluated as catalase- and SOD-like activity.[59−62]

3.2.1. Antiamyloidogenic Potential of Fe_3O_4/CeO_2 NPs.

The ability to affect protein amyloid aggregation, i.e., to inhibit the process of fibril formation and to destabilize preformed mature amyloid fibrils, has been described previously for both Fe_3O_4 and CeO_2 NPs.[17,18,22,63] However, as far as we know, no such work has been performed using Fe_3O_4/CeO_2 NCPs. We hypothesized that a combination of magnetite core and shell of CeO_2, when designed, may result in significantly enhanced antiamyloidogenic activity. Insulin was chosen to study the antiamyloidogenic effect of fabricated NPCs because it is a well-known model protein commonly used to study amyloidogenesis.[64,65]

To prove our hypothesis, we performed dose-dependent and kinetic experiments. Within a wide range of concentrations, the NCPs were added (i) to the solution of 25 μM (145 μg/mL) native insulin (inhibiting measurements) and (ii) to the dispersion of preformed fibrils in 100 mM NaCl, pH 1.6 (disassembly measurements), and samples were incubated at conditions described in the Materials and Methods section. ThT fluorescence assay has been used to determine the extent of insulin fibrillization alone and in the presence of NCPs. It is well-known that a decrease in the ThT fluorescence of inhibitor-containing samples in comparison to control insulin samples (taken as 100%) indicates a decrease in the number of amyloid fibrils as a result of the inhibition/disassembly potential of NCPs.[66,67] Figure 6 shows the dependence of ThT fluorescence as a function of the NCPs concentration; ThT fluorescence for inhibition measurements is presented in panel A, and ThT fluorescence intensities obtained for disassembly measurements are presented in panel B. The experimental data observed for Fe_3O_4 NPs forming the core of bimetal particles revealed neither strong inhibition nor strong disassembly. The effect in both cases did not exceed ∼50%. On the other hand, as shown in Figure 6, the presence of core/shell NPs led to a readily detectable decrease of the relative ThT fluorescence intensity, and the observed effect exhibited a clear dose-dependent pattern.

From the sigmoidal curves fitted to the experimental data, the apparent IC_{50} (reflecting the concentration of the NCPs concentration leading to 50% inhibition of amyloid fibrillization) and DC_{50} (the NCPs concentration leading to 50% disassembly of preformed fibrils) values were calculated. The apparent IC_{50} and DC_{50} values are summarized in Table 4. It appears that the calculated IC_{50} and DC_{50} values exhibited a size-dependent tendency; i.e., the extent of antiamyloid activity depended on the properties of NCPs, mainly on the size of NCPs, which was determined by the shell formed by CeO_2 particles. It is interesting to note that the size-dependent effects of inhibition and disassembly had the opposite trend. While the most effective inhibition activity was observed for the NCPs with a larger shell thickness, the most effective disassembly activity was observed for the smallest NCPs.

https://doi.org/10.1021/acsami.3c10845
ACS Appl. Mater. Interfaces 2023, 15, 49346−49361

Table 4. Experimentally Determined IC_{50} and DC_{50} Values for the Studied Fe_3O_4/CeO_2 NCPs

particle	antiamyloid activity (μg/mL)	
	IC_{50}	DC_{50}
Fe_3O_4	N/D	N/D
Fe_3O_4/CeO_2 -3	135 ± 6	115 ± 10
Fe_3O_4/CeO_2 -5	130 ± 2.5	215 ± 13
Fe_3O_4/CeO_2 -7	25 ± 1	250 ± 16.5
CeO_2	270 ± 13[a]	N/D

[a]Taken from ref 68.

The IC_{50} concentration of the last listed Fe_3O_4/CeO_2 NCPs was found to be ∼10 times lower (i.e., 10 times more effective inhibition) in comparison to that of pure CeO_2, and even the smallest Fe_3O_4/CeO_2 NCPs possessed ∼2 times lower IC_{50} compared to those of pure CeO_2 NPs (Table 4[17,68]). A sharp decrease in IC_{50}, especially for **Fe_3O_4/CeO_2-7**, led us to verify the ThT fluorescence data using another fluorescence dye, ANS. The obtained ANS results fully confirmed the results of the fluorescence analysis (data not shown). Because pure CeO_2 did not show such an effective inhibition potential,[17,18,22,68] it is tempting to speculate that the significantly enhanced inhibition activity of core/shell NPs, especially for **Fe_3O_4/CeO_2-7** NPs, may be a result of "chemistry" between Fe_3O_4 and CeO_2.

To better understand the process that underlies inhibition, in addition to concentration-dependent experiments, a kinetic study of insulin fibrillization in the presence of core/shell NCPs at two different concentrations was performed. The NCPs concentrations were selected considering the calculated IC_{50} values and correspond to the 1:1 and 1:0.5 (w/w) ratios (protein to NCPs; the concentration of protein was fixed and equal to 25 μM = 145 μg/mL). The kinetic time-dependent process of protein amyloid formation, referred to as nucleation-dependent polymerization, has a typical sigmoidal profile with three distinct stages: a lag phase, a growth phase, and a final steady-state phase. As documented in Figure 7, the insulin fibrillization in the absence of NCPs (gray circles) consisted of an ∼8−10-min-long lag phase followed by about a 40-min-long elongation phase. Finally, after ∼60 min, the process culminated with the plateau (or steady-state) phase, which reflected the presence of a characteristic amyloid cross-β structure. In the presence of different NCPs, the sigmoidal shape of the time-dependenct curve was generally well-preserved. However, as shown in Figure 7, the core/shell NCPs affect the kinetic profile and the extent of insulin fibrillization in a concentration-dependent manner. A more pronounced effect on the kinetics with a detectable long lag phase and a reduced extent of fibrillization was observed at a 1:1 (w/w) protein-to-NCPs ratio. The most significant inhibition of insulin fibrillogenesis was observed for **Fe_3O_4/CeO_2-7** NCPs, with a 2-fold prolonged lag phase accompanied by a remarkable decrease in the ThT fluorescence intensities. As documented in Figure 7, in the presence of **Fe_3O_4/CeO_2-7** NCPs, shallow S curves were observed, and ThT fluorescence reached approximately ∼15% and ∼43−45% of the control samples at protein-to-NCPs ratios of 1:1 and 1:0.5 (w/w), respectively. On the other hand, for NPs with the smallest CeO_2 shell characterized by a higher IC_{50} value, only a moderately changed curve profile was observed compared to those of the control insulin samples. The ThT fluorescence intensities at the plateau phase reached ∼53% (ratio 1:1) and ∼77% (ratio 1:0.5). As expected, the lowest potential to affect insulin fibrillization exhibits pure Fe_3O_4 particles. As mentioned above, this lower ability to affect the formation of protein amyloid fibrils is a result of the instability of pure Fe_3O_4 particles, which tend to form clusters. Clustering of Fe_3O_4 particles reduces the interaction with insulin molecules, which is a prerequisite for inhibiting the process.

Contrary to the inhibition experiments, the highest disassembly activity was determined for the smallest Fe_3O_4/CeO_2 NCPs; i.e., the ability to disrupt amyloid fibrils decreases with an increase in the theoretical thickness of the CeO_2 shell. Similarly, the size-dependent efficacy of altering protein amyloidogenesis for other types of NPs, including superparamagnetic iron oxide NPs or gold NPs, has previously been documented, and the important interplay between the NPs size and surface chemistry has been emphasized.[13,57,58,69,70] In addition, the obtained results confirm our previously published data, that the magnetite core is quite effective in the disaggregation of preformed fibrils,[12] while pure CeO_2 particles possess a low ability to disassemble preformed amyloid fibrils.[17,18,22] On the other hand, the antiamyloidogenic activity

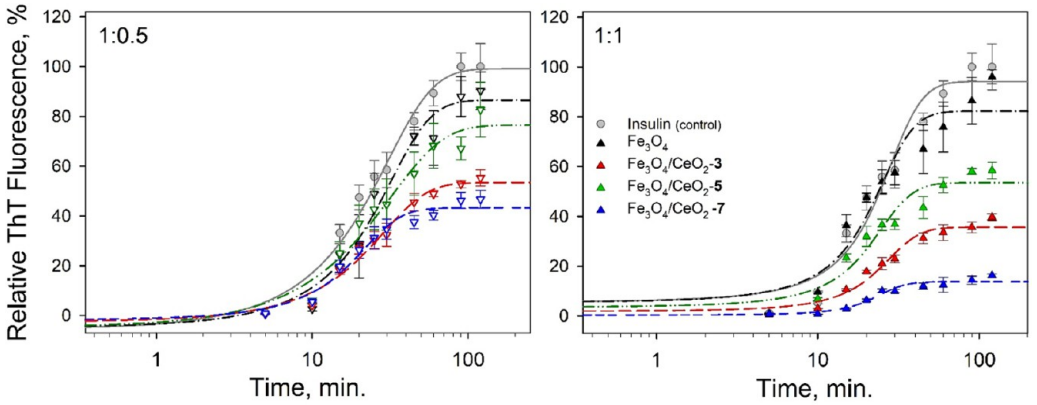

Figure 7. Time dependence of insulin fibrillization in the presence of core/shell NCPs monitored by ThT assay. The NPs at two different protein-to-NCPs ratios, 1:0.5 (w/w; empty triangles) and 1:1 (w/w; filled up-triangles), respectively, were added to a freshly prepared insulin solution, and samples were exposed to fibrillization conditions. The ThT fluorescence data in the presence of NPs were normalized to fluorescence intensities recorded after complete fibrillization of insulin alone (gray circles; taken as 100%). Each experiment was performed in triplicate; error bars represent the average deviation for repeated measurements of three separate samples.

https://doi.org/10.1021/acsami.3c10845
ACS Appl. Mater. Interfaces 2023, 15, 49346−49361

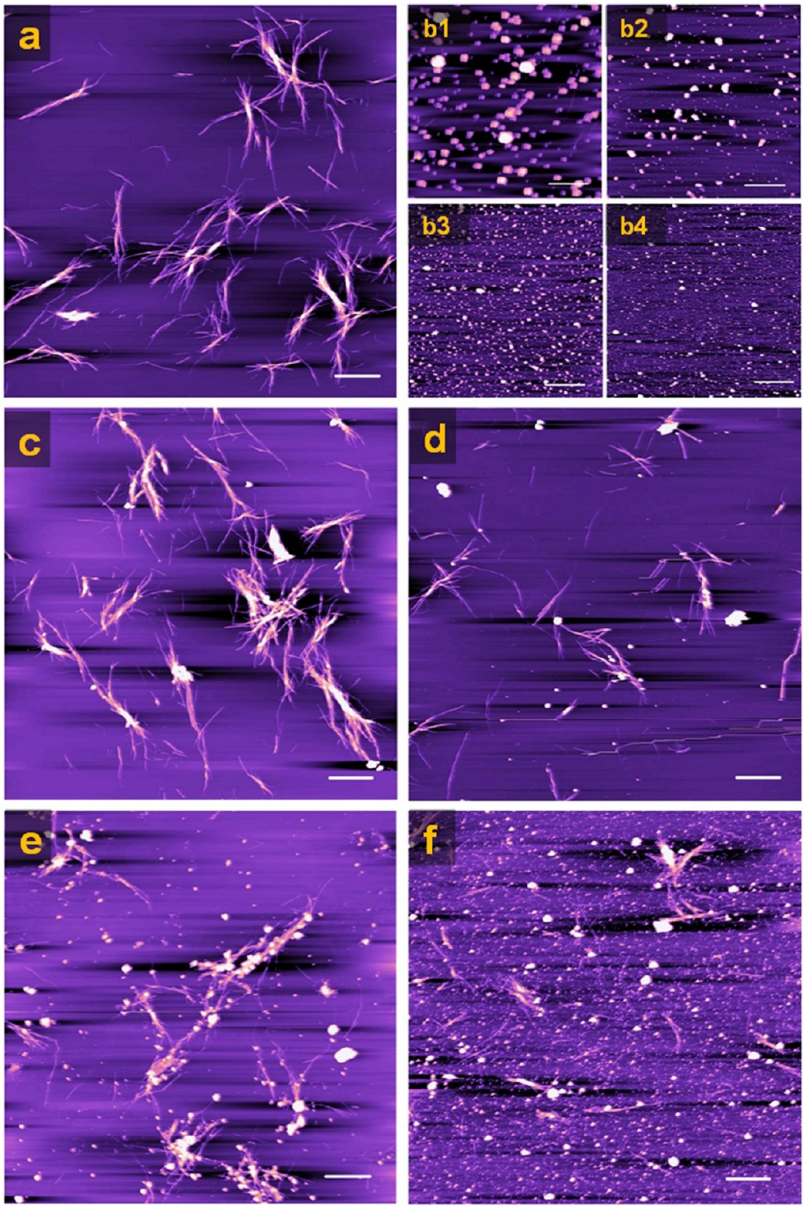

Figure 8. AFM visualization of insulin amyloid fibrils formed alone (a) and in the presence of Fe_3O_4 NPs (c), **Fe_3O_4/CeO_2-3** (d), **Fe_3O_4/CeO_2-5** (e), and **Fe_3O_4/CeO_2-7** (f) with a protein-to-NCPs ratio of 1:0.5. b1−b4 represent scans of studied NCPs (72.5 μg/mL). White scale bars always represent 1 μm. The images were processed by using *NanoScope Analysis 1.20* software.

of pure magnetite NPs used as the "core" was not so significant compared to the inhibition/disassembly potential of the core/shell NPs, and it was impossible to correctly determine the values of IC_{50} and DC_{50}. Such a low ability to affect insulin amyloid aggregation may be a result of the insufficient colloidal stability of pure Fe_3O_4. These observations indicate the importance of the magnetite core and its stabilization by the CeO_2 shell in the antiamyloidogenic activity.

Visualization of insulin fibrils using AFM was used to verify the antiamyloidogenic activity of the "core/shell" NPs observed using "indirect" ThT analysis. As documented in Figure 8a, insulin forms thin, long, unbranched fibrils. When fibrillization was performed in the presence of pure Fe_3O_4 NPs, the morphology of fibrils remained almost the same, and the characteristic amyloid morphology without significant visible changes was found (Figure 8c). In the presence of core/shell NPs (the protein-to-NCPs ratio was 1:0.5), gradual changes of both the number and morphology of fibrils were observed. The most significant inhibition of insulin amyloid formation occurred in the presence of **Fe_3O_4/CeO_2-7** NCPs (Figure 8f), and only small short fibrils were detected. A less pronounced inhibition effect on the formation of insulin fibrils was found in the presence of **Fe_3O_4/CeO_2-3** and **Fe_3O_4/CeO_2-5** NCPs (Figure 8d,e). Scans b1−b4 represent a visualization of NCPs as follows: b1, Fe_3O_4; b2, **Fe_3O_4/CeO_2-3**; b3, **Fe_3O_4/CeO_2-5**; b4, **Fe_3O_4/CeO_2-7**. Scan b1 clearly shows the clustering of pure Fe_3O_4. A certain degree of clusterization was observed also for **Fe_3O_4/CeO_2-3** NCPs (Figure 8b2), which may be explained by a nonhomogenous shell of CeO_2. AFM measurements fully confirmed the results obtained by ThT fluorescence assay.

3.2.2. Examination of the Pseudoenzymatic Activity of Fe_3O_4/CeO_2 NCPs. To assess the impact of the size/redox state on the bioactivity, we also analyzed the pseudoenzymatic

https://doi.org/10.1021/acsami.3c10845
ACS Appl. Mater. Interfaces 2023, 15, 49346−49361

activity of NCPs by monitoring the SOD-, oxidase-, and catalase-like activity. To examine the catalase- and oxidase-like activity of the studied NPs, a colorimetric assay based on the oxidation of DPD as a substrate was employed.[38] In Figure 9a,

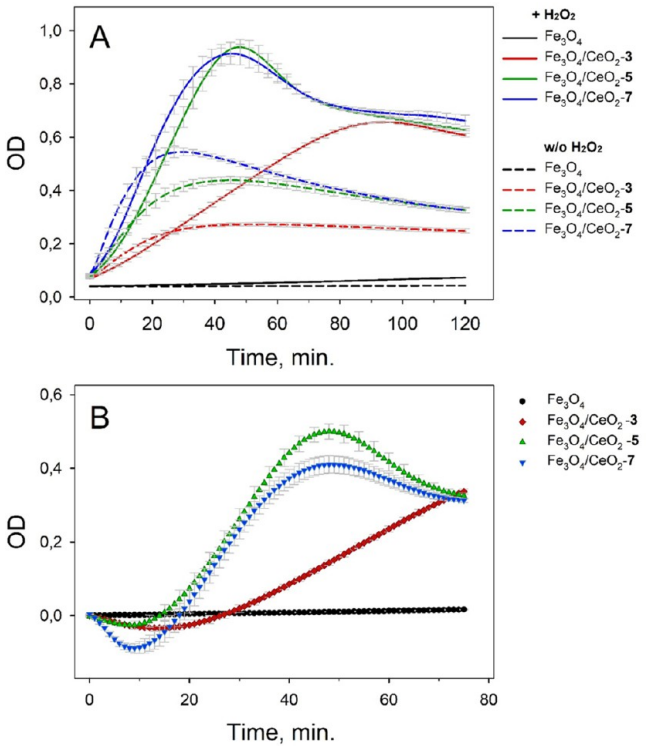

Figure 9. Monitoring of the enzyme-like activities of core/shell NCPs: (A) monitoring of the DPD oxidation by NCPs in the presence of H_2O_2 (solid lines) and the absence of H_2O_2 (short-dashed lines); (B) "true" catalase-like activity of H_2O_2 decomposition by core/shell NCPs (the curves were obtained by subtraction of the kinetic curves without H_2O_2 from the kinetic curves with $H_2O)_2$. Error bars represent the standard deviations of three independent experiments. The concentration of the NPs/NCPs was always 10 μg/mL.

the solid curves represent the oxidation of DPD in the presence of H_2O_2 and NCPs. In the presence of **Fe_3O_4/CeO_2-5** and **Fe_3O_4/CeO_2-7**, almost identical kinetic curves of H_2O_2 decomposition were obtained. However, in the presence of **Fe_3O_4/CeO_2-3**, the kinetic curve was much slower. In the absence of H_2O_2, the oxidation of DPD is shown as short-dashed curves. This pseudo-oxidase activity of NCPs arises from a low redox potential of the CeO_2 shell and the presence of oxygen vacancies as proposed previously.[22,61,62] As expected, the oxidase-like activity increases with the increased shell of CeO_2 on the magnetite core. By subtraction of the kinetic curves in the absence of H_2O_2 from the kinetic curves measured with H_2O_2, the "real" catalase-like activity of NCPs was obtained (Figure 9b). It seems that **Fe_3O_4/CeO_2-5** exhibited slightly higher catalase-like activity in comparison to **Fe_3O_4/CeO_2-7**, but the difference was very small. Although we can assume that the major catalytic activity arises from the shell of the particles, the involvement of the magnetite core cannot be excluded because XPS analysis revealed the coexistence of two redox-ion couples, Fe^{3+}/Fe^{2+} and Ce^{3+}/Ce^{4+}, and, in addition, the CeO_2 "shell" is probably not completely uniform. The coupling of both Fe_3O_4 and CeO_2 results in a higher catalytic activity than either of them alone probably due to a synergistic catalytic mechanism. Similarly, the synergistic catalase/peroxidase-like activity of CeO_2/Fe_3O_4 NCPs was observed previously, and a detailed mechanism of catalysis was described.[27,31] Moreover, the catalytic properties of core/shell NPs can be further enhanced by the appropriate coating, as shown by Moskvin et al. for magnetic γ-Fe_2O_3/CeO_x when poly(ethylene glycol)−neridronate is used.[32] Fe_3O_4 alone did not exhibit catalase-like activity due to the low stability of NPs.

To obtain a more detailed view of the enzymatic mimetic activity, the prepared core/shell NCPs were tested by using a commercial colorimetric SOD kit. SOD catalyzes the dismutation of the superoxide anion into H_2O_2 and molecular oxygen, which consequently leads to a decrease of WST-1 monitored by absorbance at 450 nm. The studied core/shell NCPs at a final concentration of 75 μg/mL were added to well plates with WST-1 reagent. Generation of the superoxide radical anions was initiated by adding xanthine oxidase. The nascent superoxide radicals reduced a water-soluble tetrazolium salt to formazan. The SOD-like activity of CeO_2 NPs was calculated from a calibration curve obtained by using the SOD kit enzyme and is expressed as the units of SOD activity (Table 5). As expected, there is no SOD-like activity for pure Fe_3O_4

Table 5. SOD-Like Activity of Fe_3O_4/CeO_2 NCPs Monitored Using an SOD Kit

	SOD activity	
	inhibition rate (%)	U/mL
Fe_3O_4	NA	NA
Fe_3O_4/CeO_2 -3	20.9 ± 2.0	1.02 ± 0.0015
Fe_3O_4/CeO_2 -5	23.03 ± 4.2	1.16 ± 0.07
Fe_3O_4/CeO_2 -7	49.8 ± 4.95	3.31 ± 0.11
CeO_2	33.3 ± 2.6	1.87 ± 0.002

NPs due to insufficient colloidal stability of pure Fe_3O_4 particles. **Fe_3O_4/CeO_2-3** and **Fe_3O_4/CeO_2-5** showed almost the same SOD-like activity. Significantly higher, more than 2-fold, SOD-like activity was observed for **Fe_3O_4/CeO_2-7**. This observation is not surprising because the SOD activity is directly related to the Ce^{3+} ions and is consistent with the analysis of the XPS spectra. XPS analysis revealed that the $w_{at.}(Ce^{3+})/w_{at.}(Ce^{4+})$ and $w_{at.}(Ce)/w_{at.}(Fe)$ (Table 1) of **Fe_3O_4/CeO_2-3** and **Fe_3O_4/CeO_2-5** are almost similar. However, for **Fe_3O_4/CeO_2-7**, both $w_{at.}(Ce^{3+})/w_{at.}(Ce^{4+})$ and $w_{at.}(Ce)/w_{at.}(Fe)$ are significantly higher. It is noteworthy that this enzymatic activity was higher compared to that of pure CeO_2.

Currently, we cannot fully explain these observations, but the calculated ∼10 times lower IC_{50} concentration and ∼1.5 times higher SOD-like activity of **Fe_3O_4/CeO_2-7** NPCs compared to those of pure CeO_2 NPs indicated a possible synergistic effect, probably due to the interaction between Fe and Ce ions. We believe that one of the solutions to understanding this phenomenon is to fabricate NCPs with a thickened (>7) outer layer around the magnetic core and evaluate the antiamyloidogenic and antioxidative activities to clarify whether such an effect is observed for the composite with the defined proportion of the components. This work is currently underway.

In any case, together with the magnetic properties of Fe_3O_4/CeO_2 NCPs and a significant improvement in the inhibition of amyloid formation and a higher SOD-like activity of **Fe_3O_4/**

https://doi.org/10.1021/acsami.3c10845
ACS Appl. Mater. Interfaces 2023, 15, 49346−49361

CeO_2-7 NPCs compared to pure CeO_2 NPs, an excellent option for delivering these NCP_S to the object of interest is proposed.

CONCLUSIONS

To clarify the possibility of combining the ability to heat up effectively in AMF and antioxidant activity in one NCP material, a set of Fe_3O_4/CeO_2 "core/shell"-like NCPs were synthesized by precipitation of the CeO_2 "shell" on the prefabricated Fe_3O_4 NPs. The amount of CeO_2 required to obtain a certain thickness of the outer shell was theoretically calculated before synthesis. The XRD, XPS, and HRTEM data revealed the coexistence of Fe_3O_4 and CeO_2 NPs in one NCP. According to the XPS spectra, the percentage of CeO_2 on the surface of the NCPs increased with growth of the CeO_2 calculated "shell", which suggested the formation of "core/shell" structures. Such an assumption was validated by HRTEM and EELS measurements, and the obtained data showed that Fe_3O_4 NPs are neatly surrounded by ultrafine CeO_2 NPs with an average size of 3−3.5 nm. Semiquantitative calculations of the XPS spectra of Fe_3O_4/CeO_2 NCPs demonstrated that the appearance of the CeO_2 "shell" around Fe_3O_4 NPs promotes a partial reduction of Fe^{3+} to Fe^{2+} ions and provides some protection of Fe_3O_4 magnetic NPs against oxidation. DLS results demonstrated that the presence of the CeO_2 "shell" significantly enhanced the stability of fabricated Fe_3O_4/CeO_2 NCPs: **Fe_3O_4/CeO_2-5** and **Fe_3O_4/CeO_2-7** NCPs possess ζ-potential values higher than +30 mV, which defines them as highly stable in the aqueous suspensions. The combined results indicated the formation of "core/shell"-like Fe_3O_4/CeO_2 composites during the synthesis. Additionally, the appearance of the CeO_2 "shell" around Fe_3O_4 NPs positively affects their magnetic properties and stability against oxidation. Despite the decrease in the magnetization values of composites with an increase in the CeO_2 content in the "shell", magnetic liquids based on Fe_3O_4/CeO_2 NCPs demonstrated their ability to heat efficiently in AMF, and the heating efficiency decreased with an increase in the percentage of CeO_2 in NCPs. The data obtained showed that the magnetic properties of the shell, depending on the thickness, determine the effectiveness of hyperthermia, which is important for understanding local temperature fluctuations, as well as for designing and fine-tuning applications in theranostics. There was significant improvement in both the antioxidant and antiamyloidogenic activity. It was found that the inhibition concentration of IC_{50} NCPs with a "shell thickness" of 7 nm is ∼10 times lower (i.e., 10 times more effective inhibition) than that of pure CeO_2. For this NCP, a more than 2 times higher SOD-like activity was observed. The combination of both Fe_3O_4 and CeO_2 leads to a higher biological activity than either of them probably due to a synergistic catalytic mechanism.

Overall, we can conclude that newly prepared bimetal NCPs demonstrate both strong antioxidant and strong antiamyloidogenic activity in a concentration- and size-dependent manner.

AUTHOR INFORMATION

Corresponding Authors

Yuliia Shlapa − *V. I. Vernadsky Institute of General and Inorganic Chemistry of the National Academy of Sciences of Ukraine, Kyiv 03142, Ukraine;* orcid.org/0000-0002-1732-0962; Email: yuliashlapa@ukr.net

Andrey Musatov − *Institute of Experimental Physics, Slovak Academy of Sciences, Kosice 04001, Slovakia;* orcid.org/0000-0001-8991-2468; Email: musatov@saske.sk

Authors

Katarina Siposova − *Institute of Experimental Physics, Slovak Academy of Sciences, Kosice 04001, Slovakia;* orcid.org/0000-0003-2778-5023

Katerina Veltruska − *Department of Surface and Plasma Science, Faculty of Mathematics and Physics, Charles University, Prague 8 18000, Czech Republic*

Valentin-Adrian Maraloiu − *National Institute of Materials Physics, Magurele 077125, Romania;* orcid.org/0000-0002-4400-5060

Ivana Garcarova − *Institute of Experimental Physics, Slovak Academy of Sciences, Kosice 04001, Slovakia*

Michal Rajnak − *Institute of Experimental Physics, Slovak Academy of Sciences, Kosice 04001, Slovakia;* orcid.org/0000-0002-1308-9513

Anatolii Belous − *V. I. Vernadsky Institute of General and Inorganic Chemistry of the National Academy of Sciences of Ukraine, Kyiv 03142, Ukraine*

Complete contact information is available at: https://pubs.acs.org/10.1021/acsami.3c10845

Notes

The authors declare no competing financial interest.

ACKNOWLEDGMENTS

This work was performed in the framework of the "Grants of the NAS of Ukraine to research laboratories/groups of young scientists of the NAS of Ukraine" (Project 0121U110363) and Program from The Institute of Electrical and Electronics Engineers Magnetics Society "Magnetism for Ukraine 2022" (Project 9918) and supported by research grants from the NATO Science for Peace and Security Program (G5683), Slovak Grant Agency VEGA (Nos. 2/0094/21 and 2/0034/22), Slovak Research and Development Agency (APVV-19-0324), and SAS-MOST JRP 2021/2 (AZCAI). The authors acknowledge the CERIC−ERIC Consortium for access to experimental facilities and the possibility to perform XPS measurements in the framework of Grant 20217038 and HRTEM measurements within Grant No20207013. This work was also partially supported by a grant from the Czech Ministry of Education Youth and Sports (Project LM 2023072) and a grant from the Romanian Ministry of Research, Innovation, and Digitization, CNCS-UEFISCDI (Project PN-III-P1-1.1-TE-2021-0981) within PNCDI III. We thank Dagmar Sedlakova (Institute of Experimental Physics, SAS, Kosice, Slovakia) for her technical assistance.

REFERENCES

(1) Joudeh, N.; Linke, D. Nanoparticle Classification, Physicochemical Properties, Characterization, and Applications: A Comprehensive Review for Biologists. *J. Nanobiotechnol.* **2022**, *20* (1), 1−29.

(2) Liu, X.; Li, S.; Li, Z.; Cao, F.; Su, L.; Shtansky, D. V.; Fang, X. Enhanced Response Speed in 2D Perovskite Oxides-Based Photodetectors for UV Imaging through Surface/Interface Carrier-Transport Modulation. *ACS Appl. Mater. Interfaces* **2022**, *14* (43), 48936−48947.

(3) Holzinger, M.; Le Goff, A.; Cosnier, S. Nanomaterials for Biosensing Applications: A Review. *Front. Chem.* **2014**, *2*, 63.

(4) Ashik, U. P. M.; Viswan, A.; Kudo, S.; Hayashi, J. I. (2018). Nanomaterials as Catalysts. *Applicat. Nanomater* **2018**, 45−82.

(5) Vangijzegem, T.; Stanicki, D.; Laurent, S. Magnetic Iron Oxide Nanoparticles for Drug Delivery: Applications and Characteristics. *Expert Opin. Drug Delivery* **2019**, *16* (1), 69−78.
(6) Laurent, S.; Dutz, S.; Häfeli, U. O.; Mahmoudi, M. Magnetic Fluid Hyperthermia: Focus on Superparamagnetic Iron Oxide Nanoparticles. *Adv. Colloid Interface Sci.* **2011**, *166* (1−2), 8−23.
(7) Canaparo, R.; Foglietta, F.; Limongi, T.; Serpe, L. Biomedical Applications of Reactive Oxygen Species Generation by Metal Nanoparticles. *Materials* **2021**, *14* (1), 53.
(8) Kaczmarek, K.; Hornowski, T.; Dobosz, B.; Józefczak, A. Influence of Magnetic Nanoparticles on the Focused Ultrasound Hyperthermia. *Materials* **2018**, *11*, 1607.
(9) Jozefczak, A.; Kaczmarek, K.; Hornowski, T.; Kubovcikova, M.; Rozynek, Z.; Timko, M.; Skumiel, A. Magnetic Nanoparticles for Enhancing the Effectiveness of Ultrasonic Hyperthermia. *Appl. Phys. Lett.* **2016**, *108*, No. 263701.
(10) Zhang, Y.; Wang, Y.; Zhou, Q.; Chen, X.; Jiao, W.; Li, G.; Peng, M.; Liu, X.; He, Y.; Fan, H. Precise Regulation of Enzyme−Nanozyme Cascade Reaction Kinetics by Magnetic Actuation toward Efficient Tumor Therapy. *ACS Appl. Mater. Interfaces* **2021**, *13*, 52395−52405.
(11) Skaat, H.; Shafir, G.; Margel, S. Acceleration and Inhibition of Amyloid-β Fibril Formation by Peptide-Conjugated Fluorescent-Maghemite Nanoparticles. *J. Nanopart. Res.* **2011**, *13*, 3521−3534.
(12) Siposova, K.; Kubovcikova, M.; Bednarikova, Z.; Koneracka, M.; Zavisova, V.; Antosova, A.; Kopcansky, P.; Daxnerova, Z.; Gazova, Z. Depolymerization of Insulin Amyloid Fibrils by Albumin-Modified Magnetic Fluid. *Nanotechnol* **2012**, *23*, No. 055101.
(13) Mahmoudi, M.; Quinlan-Pluck, F.; Monopoli, M. P.; Sheibani, S.; Vali, H.; Dawson, K. A.; Lynch, I. Influence of the Physiochemical Properties of Superparamagnetic Iron Oxide Nanoparticles on Amyloid β Protein Fibrillation in Solution. *ACS Chem. Neurosci.* **2013**, *4*, 475−485.
(14) Andrikopoulos, N.; Song, Z.; Wan, X.; Douek, A. M.; Javed, I.; Fu, C.; Xing, Y.; Xin, F.; Li, Y.; Kakinen, A.; Koppel, K.; Qiao, R.; Whittaker, A. K.; Kaslin, J.; Davis, T. P.; Song, Y.; Ding, F.; Ke, P. C. Inhibition of Amyloid Aggregation and Toxicity with Janus Iron Oxide Nanoparticles. *Chem. Mater.* **2021**, *33* (16), 6484−6500.
(15) Weaver, J. D.; Stabler, C. L. Antioxidant Cerium Oxide Nanoparticle Hydrogels for Cellular Encapsulation. *Acta Biomater.* **2015**, *16*, 136−144.
(16) Sarnatskaya, V.; Shlapa, Yu.; Yushko, L.; Shton, I.; Solopan, S.; Ostrovska, G.; Kalachniuk, L.; Negelia, A.; Garmanchuk, L.; Prokopenko, I.; Khudenko, N.; Maslenny, V.; Bubnovskaya, L.; Belous, A.; Nikolaev, V. Biological Activity of Cerium Dioxide Nanoparticles. *J. Biomed. Mater. Res.* **2020**, *108*, 1703−1712.
(17) Siposova, K.; Huntosova, V.; Shlapa, Yu.; Lenkavska, L.; Macajova, M.; Belous, A.; Musatov, A. Advances in the Study of Cerium Oxide Nanoparticles: New Insights into Antiamyloidogenic Activity. *ACS Appl. Bio Mater.* **2019**, *2* (5), 1884−1896.
(18) Siposova, K.; Huntosova, V.; Garcarova, I.; Shlapa, Yu.; Timashkov, I.; Belous, A.; Musatov, A. Dual-Functional Antioxidant and Anti-amyloid Cerium Oxide Nanoparticles Fabricated by Controlled Synthesis in Water-Alcohol Solutions. *Biomedicines* **2022**, *10*, 942.
(19) Kannan, K.; Radhika, D.; Sadasivuni, K. K.; Reddy, K. R.; Raghu, A. V. Nanostructured Metal Oxides and Its Hybrids for Photocatalytic and Biomedical Applications. *Adv. Colloid Interface Sci.* **2020**, *281*, No. 102178.
(20) Heckert, E. G.; Karakoti, A. S.; Seal, S.; Self, W. T. The Role of Cerium Redox State in the SOD Mimetic Activity of Nanoceria. *Biomaterials* **2008**, *29* (18), 2705−2709.
(21) Lee, S. S.; Song, W.; Cho, M.; Puppala, H. L.; Nguyen, P.; Zhu, H.; Segatori, L.; Colvin, V. L. (2013). Antioxidant Properties of Cerium Oxide Nanocrystals as a Function of Nanocrystal Diameter and Surface Coating. *ACS Nano* **2013**, *7* (11), 9693−9703.
(22) Shlapa, Yu.; Solopan, S.; Sarnatskaya, V.; Siposova, K.; Garcarova, I.; Veltruska, K.; Timashkov, I.; Lykhova, O.; Kolesnik, D.; Musatov, A.; Nikolaev, V.; Belous, A. Cerium Dioxide Nanoparticles Synthesized via Precipitation at Constant pH: Synthesis, Physical-Chemical and Antioxidant Properties. *Colloids Surf. B Biointerface* **2022**, *220*, No. 112960.
(23) Ghosh Chaudhuri, R.; Paria, S. Core/Shell Nanoparticles: Classes, Properties, Synthesis Mechanisms, Characterization, and Applications. *Chem. Rev.* **2012**, *112* (4), 2373−2433.
(24) Zhu, N.; Ji, H.; Yu, P.; Niu, J.; Farooq, M. U.; Akram, M. W.; Udego, I. O.; Li, H.; Niu, X. Surface Modification of Magnetic Iron Oxide Nanoparticles. *Nanomaterials* **2018**, *8* (10), 810.
(25) Gao, S.; Zhang, W.; An, Z.; Kong, S.; Chen, D. (2019). Adsorption of Anionic Dye onto Magnetic Fe_3O_4/CeO_2 Nanocomposite: Equilibrium, Kinetics, and Thermodynamics. *Adsorp. Sci. Technol.* **2019**, *37* (3−4), 185−204.
(26) Xu, L.; Wang, J. Magnetic Nanoscaled Fe_3O_4/CeO_2 Composite as an Efficient Fenton-Like Heterogeneous Catalyst for Degradation of 4-Chlorophenol. *Environ. Sci. Technol.* **2012**, *46* (18), 10145−10153.
(27) Wei, J.; Yao, H.; Wang, Y.; Luo, G. Controllable Preparation and Catalytic Performance of Magnetic Fe_3O_4@CeO_2-Polysulfone Nanocomposites with Core−Shell Structure. *Ind. Eng. Chem. Res.* **2018**, *57* (44), 15039−15045.
(28) Rizzuti, A.; Dipalo, M. C.; Allegretta, I.; Terzano, R.; Cioffi, N.; Mastrorilli, P.; Mali, M.; Romanazzi, G.; Nacci, A.; Dell'Anna, M. M. Microwave-Assisted Solvothermal Synthesis of Fe_3O_4/CeO_2 Nanocomposites and Their Catalytic Activity in the Imine Formation from Benzyl Alcohol and Aniline. *Catalysts* **2020**, *10* (11), 1325.
(29) Wu, Y.; Yang, Y.; Zhao, W.; Xu, Z. P.; Little, P. J.; Whittaker, A. K.; Zhang, R.; Ta, H. T. Novel Iron Oxide−Cerium Oxide Core−Shell Nanoparticles as a Potential Theranostic Material for ROS Related Inflammatory Diseases. *J. Mater. Chem. B* **2018**, *6* (30), 4937−4951.
(30) Lee, C. R.; Kim, G. G.; Park, S. B.; Kim, S. W. Synthesis of Hyaluronic Acid-Conjugated Fe_3O_4@CeO_2 Composite Nanoparticles for a Target-Oriented Multifunctional Drug Delivery System. *Micromachines* **2021**, *12*, 1018.
(31) Huang, F.; Wang, J.; Chen, W.; Wan, Y.; Wang, X.; Cai, N.; Liu, J.; Yu, F. Synergistic Peroxidase-Like Activity of CeO_2-Coated Hollow Fe_3O_4 Nanocomposites as an Enzymatic Mimic for Low Detection Limit of Glucose. *J. Taiwan Inst. Chem. Eng.* **2018**, *83*, 40−49.
(32) Moskvin, M.; Markova, I.; Malinska, H.; Miklankova, D.; Huttl, M.; Oliyarnyk, O.; Pop-Georgievski, O.; Zhigunov, A.; Petrovsky, E.; Horak, D. Cerium Oxide-Decorated γ-Fe_2O_3 Nanoparticles: Design, Synthesis and *in vivo* Effects on Parameters of Oxidative Stress. *Front. Chem.* **2020**, *8*, 682.
(33) Yelenich, O. V.; Solopan, S. O.; Kolodiazhnyi, T. V.; Greneche, J. M.; Belous, A. G. Synthesis of Iron Oxide Nanoparticles by Different Methods and Study of their Properties. *Solid State Phenom.* **2015**, *230*, 108−113.
(34) Solopan, S. O.; Nedelko, N.; Lewinska, S.; Slawska-Waniewska, A.; Zamorskyi, V. O.; Tovstolytkin, A. I.; Belous, A. G. Core/Shell Architecture as an Efficient Tool to Tune DC Magnetic Parameters and AC Losses in Spinel Ferrite Nanoparticles. *J. Alloys Compd.* **2019**, *788*, 1203−1210.
(35) Madsen, I. C.; Scarlett, N. V. Y.; Kern, A. Description and Survey of Methodologies for the Determination of Amorphous Content via X-ray Powder Diffraction. *Z. Kristallogr.* **2011**, *226*, 944−955.
(36) Holzwarth, U.; Gibson, N. The Scherrer equation versus the 'Debye-Scherrer equation'. *Nat. Nanotechnol.* **2011**, *6*, 534.
(37) Veverka, M.; Zaveta, K.; Kaman, O.; Veverka, P.; Knizek, K.; Pollert, E.; Burian, M.; Kaspar, P. Magnetic Heating by Silica-Coated Co−Zn Ferrite Particles. *J. Phys. D Appl. Phys.* **2014**, *47*, 065503−065511.
(38) Bader, H.; Sturzenegger, V.; Hoigné, J. Photometric Method for the Determination of Low Concentrations of Hydrogen Peroxide by the Peroxidase Catalyzed Oxidation of N,N-Diethyl-p-Phenylenediamine (DPD). *Water Res.* **1988**, *22*, 1109−1115.
(39) Holder, C. F.; Schaak, R. E. Tutorial on Powder X-ray Diffraction for Characterizing Nanoscale Materials. *ACS Nano* **2019**, *13* (7), 7359−7365.

https://doi.org/10.1021/acsami.3c10845
ACS Appl. Mater. Interfaces 2023, 15, 49346−49361

(40) Shard, A. G. Practical Guides for X-ray Photoelectron Spectroscopy: Quantitative XPS. *J. Vac. Sci. Technol. A: Vac., Surf. Films* **2020**, *38* (4), No. 041201.
(41) Poulin, S.; França, R.; Moreau-Bélanger, L.; Sacher, E. Confirmation of X-ray Photoelectron Spectroscopy Peak Attributions of Nanoparticulate Iron Oxides, Using Symmetric Peak Component Line Shapes. *J. Phys. Chem. C* **2010**, *114* (24), 10711−10718.
(42) McIntyre, N. S.; Zetaruk, D. G. X-ray Photoelectron Spectroscopic Studies of Iron Oxides. *Anal. Chem.* **1977**, *49* (11), 1521−1529.
(43) Tamaura, Y.; Buduan, P. V.; Katsura, T. Studies on the Oxidation of Iron (II) Ion during the Formation of Fe_3O_4 and α-FeO(OH) by Air Oxidation of $Fe[OH]_2$ Suspensions. *J. Chem. Soc., Dalton Trans.* **1981**, *9*, 1807−1811.
(44) Chen, F.; Ilyas, N.; Liu, X.; Li, Z.; Yan, S.; Fu, H. Size Effect of Fe_3O_4 Nanoparticles on Magnetism and Dispersion Stability of Magnetic Nanofluid. *Front. Energy Res.* **2021**, *9*, No. 780008.
(45) Szatkowski, T.; Wysokowski, M.; Lota, G.; Pęziak, D.; Bazhenov, V. V.; Nowaczyk, G.; Walter, J.; Molodtsov, S.; Stocker, H.; Himcinschi, C.; Petrenko, I.; Stelling, A. L.; Jurga, S.; Jesionowski, T.; Ehrlich, H. Novel Nanostructured Hematite−Spongin Composite Developed Using an Extreme Biomimetic Approach. *RSC Adv.* **2015**, *5* (96), 79031−79040.
(46) Grosvenor, A. P.; Kobe, B. A.; Biesinger, M. C.; McIntyre, N. S. (2004). Investigation of Multiplet Splitting of Fe 2p XPS Spectra and Bonding in Iron Compounds. *Surf. Interface Anal.* **2004**, *36* (12), 1564−1574.
(47) Biesinger, M. C.; Payne, B. P.; Grosvenor, A. P.; Lau, L. W.; Gerson, A. R.; Smart, R. S. C. Resolving Surface Chemical States in XPS Analysis of First Row Transition Metals, Oxides and Hydroxides: Cr, Mn, Fe, Co and Ni. *Appl. Surf. Sci.* **2011**, *257* (7), 2717−2730.
(48) Gan, G.; Zhao, P.; Zhang, X.; Liu, J.; Liu, J.; Zhang, C.; Hou, X. Degradation of Pantoprazole in Aqueous Solution Using Magnetic Nanoscaled Fe_3O_4/CeO_2 Composite: Effect of System Parameters and Degradation Pathway. *J. Alloys Compd.* **2017**, *725*, 472−483.
(49) Zhang, F.; Wang, P.; Koberstein, J.; Khalid, S.; Chan, S. W. Cerium Oxidation State in Ceria Nanoparticles Studied with X-ray Photoelectron Spectroscopy and Absorption Near Edge Spectroscopy. *Surf. Sci.* **2004**, *563* (1−3), 74−82.
(50) Beche, E.; Charvin, P.; Perarnau, D.; Abanades, S.; Flamant, G. Ce 3d XPS Investigation of Cerium Oxides and Mixed Cerium Oxide ($Ce_xTi_yO_z$). *Surf. Interface Anal.* **2008**, *40*, 264−267.
(51) Deshpande, S.; Patil, S.; Kuchibhatla, S. V. N. T.; Seal, S. Size Dependency Variation in Lattice Parameter and Valency States in Nanocrystalline Cerium Oxide. *Appl. Phys. Lett.* **2005**, *87*, No. 133113.
(52) Ismail, R. A.; Abid, S. A.; Taha, A. A. Preparation and Characterization of CeO_2@Ag Core/Shell Nanoparticles by Pulsed Laser Ablation in Water. *Lasers Manuf. Mater. Process.* **2019**, *6*, 126−135.
(53) Bhattacharjee, S. DLS and Zeta Potential − What They Are and What They Are not? 2016. *J. Controlled Release* **2016**, *235*, 337−351.
(54) Walter, A.; Garofalo, A.; Parat, A.; Martinez, H.; Felder-Flesch, D.; Begin-Colin, S. Functionalization Strategies and Dendronization of Iron Oxide Nanoparticles. *Nanotechnol. Rev.* **2015**, *4* (6), 581−593.
(55) Petrinic, I.; Stergar, J.; Bukšek, H.; Drofenik, M.; Gyergyek, S.; Hélix-Nielsen, C.; Ban, I. Superparamagnetic Fe_3O_4@CA Nanoparticles and Their Potential as Draw Solution Agents in Forward Osmosis. *Nanomaterials* **2021**, *11*, 2965.
(56) Panda, R. N.; Gajbhiye, N. S.; Balaji, G. Magnetic Properties of Interacting Single Domain Fe_3O_4 Particles. *J. Alloys Compd.* **2001**, *326* (1−2), 50−53.
(57) Sukhanova, A.; Poly, S.; Bozrova, S.; Lambert, E.; Ewald, M.; Karaulov, A.; Molinari, M.; Nabiev, I. Nanoparticles with a Specific Size and Surface Charge Promote Disruption of the Secondary Structure and Amyloid-Like Fibrillation of Human Insulin Under Physiological Conditions. *Front. Chem.* **2019**, *7*, 480.
(58) John, T.; Adler, J.; Elsner, C.; Petzold, J.; Krueger, M.; Martin, L. L.; Huster, D.; Risselada, H. J.; Abel, B. Mechanistic Insights into the Size-Dependent Effects of Nanoparticles on Inhibiting and Accelerating Amyloid Fibril Formation. *J. Colloid Interface Sci.* **2022**, *622*, 804−818.
(59) Gao, L.; Zhuang, J.; Nie, L.; Zhang, J.; Zhang, Y.; Gu, N.; Wang, T.; Feng, J.; Yang, D.; Perrett, S.; Yan, X. Intrinsic Peroxidase-Like Activity of Ferromagnetic Nanoparticles. *Nat. Nanotechnol.* **2007**, *2* (9), 577−583.
(60) Wei, H.; Wang, E. Nanomaterials with Enzyme-Like Characteristics (Nanozymes): Next- Generation Artificial Enzymes. *Chem. Soc. Rev.* **2013**, *42* (14), 6060−6093.
(61) Celardo, I.; De Nicola, M.; Mandoli, C.; Pedersen, J. Z.; Traversa, E.; Ghibelli, L. Ce^{3+} Ions Determine Redox-Dependent Anti-Apoptotic Effect of Cerium Oxide Nanoparticles. *ACS Nano* **2011**, *5*, 4537−4549.
(62) Baldim, V.; Bedioui, F.; Mignet, N.; Margaill, I.; Berret, J.-F. The Enyzme-like Catalytic Activity of Cerium Oxide Nanoparticles and Its Dependency on Ce^{3+} Surface Area Concentration. *Nanoscale* **2018**, *10*, 6971−6980.
(63) Skaat, A.; Belfort, G.; Margel, S. Synthesis and Characterization of Fluorinated Magnetic Core−Shell Nanoparticles for Inhibition of Insulin Amyloid Fibril Formation. *Nanotechnol.* **2009**, *20*, No. 225106.
(64) Akbarian, M.; Yousefi, R.; Farjadian, F.; Uversky, V. N. Insulin Fibrillation: Toward Strategies for Attenuating the Process. *Chem. Commun.* **2020**, *56*, 11354−11373.
(65) Das, A.; Shah, M.; Saraogi, I. Molecular Aspects of Insulin Aggregation and Various Therapeutic Interventions. *ACS Bio Med. Chem. Au* **2022**, *2* (3), 205−221.
(66) LeVine, H., 3rd; Thioflavine, T. Interaction with Synthetic Alzheimer's Disease Beta Amyloid Peptides: Detection of Amyloid Aggregation in Solution. *Protein Sci.* **1993**, *2*, 404−410.
(67) Xue, C.; Lin, T. Y.; Chang, D.; Guo, Z. Thioflavin T as an Amyloid Dye: Fibril Quantification, Optimal Concentration and Effect on Aggregation. *R. Soc. Open Sci.* **2017**, *4*, No. 160696.
(68) Garcarova, I.; Valusova, E.; Shlapa, Yu.; Belous, A.; Musatov, A.; Siposova, K. Surface-modified cerium dioxide nanoparticles with improved anti-amyloid and preserved nanozymatic activity. *Colloids Surf. B Biointerface* **2023**, *227*, No. 113356.
(69) Meesaragandla, B.; Karanth, S.; Janke, U.; Delcea, M. Biopolymer-Coated Gold Nanoparticles Inhibit Human Insulin Amyloid Fibrillation. *Sci. Rep.* **2020**, *10*, 7862.
(70) Gao, G.; Zhang, M.; Gong, D.; Chen, R.; Hu, X.; Sun, T. The Size-Effect of Gold Nanoparticles and Nanoclusters in the Inhibition of Amyloid-β Fibrillation. *Nanoscale* **2017**, *9*, 4107−4113.

https://doi.org/10.1021/acsami.3c10845
ACS Appl. Mater. Interfaces 2023, 15, 49346−49361